A Method for Computing Horizontal Pressure-Gradient Force in an Oceanic Model with a Non-Aligned Vertical Coordinate

Alexander F. Shchepetkin and James C. McWilliams

Institute of Geophysics and Planetary Physics, University of California at Los Angeles,
405 Hilgard Avenue, Los Angeles, CA 90095-1567 e-mail: *alex@atmos.ucla.edu* *jcm@atmos.ucla.edu*

Abstract. Discretization of the pressure-gradient force is a long-standing problem in terrain-following (or σ) coordinate oceanic modeling. When the isosurfaces of the vertical coordinate are not aligned with either geopotential surfaces or isopycnals, the horizontal pressure gradient consists of two large terms that tend to cancel; the associated pressure-gradient error stems from interference of the discretization errors of these terms. The situation is further complicated by the non-orthogonality of the coordinate system and by the common practice of using highly non-uniform stretching for the vertical grids, which, unless special precautions are taken, causes both a loss of discretization accuracy overall and an increase in interference of the component errors. In the present study we design a pressure-gradient algorithm which achieves more accurate hydrostatic balance between the two components and does not lose as much accuracy with non-uniform vertical grids at relatively coarse resolution. This algorithm is based on the reconstruction of the density field and the physical z-coordinate as continuous functions of transformed coordinates with subsequent analytical integration to compute the pressure-gradient force. This approach allows not only a formally higher order of accuracy, but it also retains and expands to high orders several important symmetries of the original second-order scheme (Mellor *et al*, 1994, Song, 1998), which is used as a prototype, as well as it has build-in monotonicity constraining algorithm which prevents appearance of spurious oscillations of polynomial interpolant, and, consequently, insures numerical stability and robustness of the model under the conditions of non-smooth density field and coarse grid resolution. We further incorporate an alternative method of dealing with compressibility of seawater which escapes pressure-gradient errors associated with interference of the nonlinear nature of equation of state and difficulties to achieve accurate polynomial fits of resultant *in situ* density profiles. In doing so, we generalized the monotonicity constraint to guarantee non-negative physical stratification of the reconstructed density profile in the case of compressible equation of state. To verify the new method, we perform traditional idealized (Seamount) and realistic test problems.

keywords:	sigma-coordinate pressure gradient error	compressibility of seawater
	high-order, monotonic interpolation	adiabatic differencing

AGU index terms:	4255	Numerical modeling
	4528	Fronts and jets
	4271	Physical and chemical properties of seawater
	4532	General circulation

Received 3 July 2001; revised 20 August 2002; accepted 5 September 2002; published 20 March 2003.

Citation: Shchepetkin, A. F., and J. C. McWilliams, A method for compu ting horizontal pressure-gradient force in an oceanic model with a non aligned vertical coordinate, *J. Geophys. Res.,* 108(C3), 3090, doi:10.1 029/2001JC001047, 2003.

where the expression in square brackets is similar to (1.1), except that P is replaced with ρ. Eq. (1.7) is then discretized in a manner similar to that described above, except that now vertical integration becomes the second step rather than the first and P never appears explicitly in the model. Because of the form of (1.7), these methods are often referred as *density-Jacobian*, opposite to the *pressure-Jacobian* family described above. The PGF schemes in two commonly used terrain-following oceanic models (POM and SCRUM)[2] belong to this class.

Song, 1998, and Song & Wright, 1998, argue that a density-Jacobian method is inherently more accurate than a pressure-Jacobian. Indeed, it is easy to see that, if the basic second-order approximations (2-point differencing, interpolation and trapezoidal integration) are used and if ρ is a linear function of z, then the error of a density-Jacobian method vanishes identically, while a linear ρ corresponds to a quadratic P; therefore, discretizations based on a linear fit for P (cf., Janjic, 1977, Lin, 1997, Janjic, T., 1998) are not able to capture this correctly resulting in hydrostatic error for this particular profile. On the other hand, Lin, 1997, argues that it is advantageous to discretize PGF using a finite-volume method. An attractive feature of this approach is that the discretized PGF naturally appears in flux-divergent form, which makes the proof of momentum and bottom-torque consistency [cf., Arakawa & Suarez, 1983; Song & Wright, 1998] simple. There is no obvious way to cast a density-Jacobian scheme into the form of a difference of P fluxes. This conflict between accuracy and conservation properties of σ-coordinate PGF schemes is not unnoticed in the literature (e.g., Beckmann & Haidvogel, 1993; Song & Wright, 1998). It is also not surprising that oceanic models tend to use density-Jacobian, while atmospheric models use pressure-Jacobian. In comparison with the atmosphere, the ocean is often more strongly stratified, and the stratification is much more spatially variable: it is not unusual to see a change of Brunt-Väisäla frequency by two orders of magnitude throughout a vertical column. While most of the vertical density gradient in atmospheric models is due to the compressibility effect, which may be absorbed by special mapping techniques as well as by the choice of vertical coordinate system (e.g., pressure instead of geopotential; Arakawa & Suarez, 1983), the relative complexity of the equation of state for seawater makes such procedures much harder in oceanic models, shifting the priority toward an accurate representation of $\rho(z)$ profiles and a preference for the density-Jacobian.

[2]POM – Princeton Ocean Model, Blumberg & Mellor, 1987; SCRUM – S-Coordinate Rutgers University Model, Song & Haidvogel, 1994.

The high-order PGF schemes available to date follow the path of straightforward discretization of (1.6) using a spectral method in the vertical direction in combination with either conventional or compact forth-order finite differences and interpolations in the horizontal (McCalpin, 1994) or spectral in combination with compact differencing up to sixth-order accuracy (Chu & Fan, 1997, 1998). The approach relies exclusively on the smallness of the truncation errors of the elementary discretizations (computation of the first derivative and mid-point interpolation), which is justifiable only when the density field is smooth on the grid scale. This is reasonably successful for idealized test problems, but practically useless for real-world simulations where fields are not smooth on affordable grids. A comprehensive comparison of performance of schemes available to date may be found in Kliem & Pietrzak, 1999, for various test problems. Although one might argue, that the analytical density profiles used in this reference are discontinuous in the first derivatives, and therefore the posedness of the problem is prejudicial against high-order methods, their inherent nonrobustness is consistent with the more general experience in realistic basin-scale simulations, resulting in the fact that, to our best knowledge, to date none of such simulations were performed using PGF scheme of higher than the basic second-order accuracy.

In the present study we describe the symmetry properties of the second-order density-Jacobian scheme and analyze sources of numerical errors. We then seek a high-order accuracy extension to this method which retains most of the symmetries and is both accurate and robust in situations where ρ changes sharply from one grid point to another with nonuniformly stretched grids. The methodology we employ is based on the reconstruction of both ρ and z as continuous functions of the transformed coordinates, which are then analytically integrated along the contours bounding the grid cells surrounding the velocity components. Since, in this approach, all steps after ρ reconstruction are exact (since ρ is treated as a continuous analytical function), the resultant algorithm can be equivalently reformulated in either Jacobian (1.7) or σ-coordinate primitive form (1.6) (reflecting the fact that these two are equivalent at the level of continuous equations), which in effect disproves the long-standing belief that a Jacobian formulation is inherently more accurate.

2. Second-order Density Jacobian

The density-Jacobian discretization is based on a con-

$\mathcal{J}(\rho,z)$ is performed, the overall PGF scheme retains positive definiteness in sense that the addition of a positive ρ perturbation at any point on one side and above the velocity point at which the PGF is evaluated always causes an increment in PGF directed away from that side, as it should be; instead it merely degrades the accuracy of the scheme. Another consequence of (2.9) is the effect of cancellation of hydrostatic error if either $z_2 = z_3$ or $z_1 = z_4$, (cf., Mellor *et al*, 1998); in this case, z_* is equal to common value of $z_2 = z_3$ or $z_1 = z_4$, and ρ interpolation to z_* becomes exact. This property is also obvious from the diagonal form (2.5).

(iii) "Pseudo-flux" form:

$$-\Delta x \Delta s\ \mathcal{J}(\rho,z) = F_{21} + F_{42} - F_{43} - F_{31}\,, \qquad (2.11)$$

where

$$\begin{aligned} F_{21} &= \frac{\rho_1+\rho_2}{2}\,(z_2-z_1) \\ F_{42} &= \frac{\rho_2+\rho_4}{2}\,(z_4-z_2) \\ F_{43} &= \frac{\rho_3+\rho_4}{2}\,(z_4-z_3) \\ F_{31} &= \frac{\rho_1+\rho_3}{2}\,(z_3-z_1)\,, \end{aligned} \qquad (2.12)$$

are called fluxes because they are shared by two grid elements adjacent either in horizontal or vertical direction. This form is not equivalent to a true finite-volume flux form (Lin, 1997), where the net force applied to a control volume element around velocity point is expressed as sum of P fluxes applied to all facets of the element; e.g., (2.11)–(2.12) does not have property that summation of PGFs applied to adjacent velocity elements can be expressed in terms of integral along the outer surface enclosing all elements included into summation. The rewriting of (2.3) into (2.11) is a discrete analog of Green's theorem,

$$\iint_{\mathcal{A}} \mathcal{J}(\rho,z)\,dx\,ds = \oint \rho(\mathbf{k},\mathbf{l})dl\,, \qquad (2.13)$$

or, more simply,

$$\iint_{\mathcal{A}} \left.\frac{\partial\rho}{\partial x}\right|_z dx\,dz = \oint \rho\,\mathbf{dz}\,, \qquad (2.14)$$

where $\mathbf{k}$ is the unit vector pointing in positive z-direction (upward) and $\mathbf{l}$ is unit vector along the contour of trapezoidal element. Eqs. (2.11)–(2.12) can be viewed as trapezoidal rule approximation to (2.14), which leads to graphical explanation of leading-order hydrostatic error second-order Jacobian resulting from terms associated with second vertical derivative of ρ (Fig. 2).

(iv) σ-coordinate primitive form:

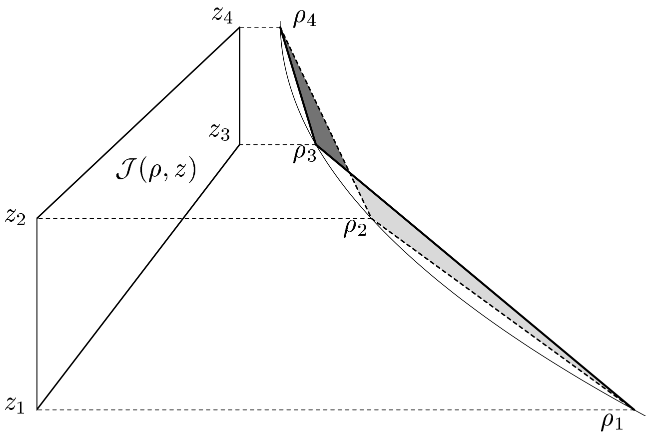

Figure 2. Explanation of appearance of hydrostatic error of second-order density-Jacobian scheme: Eqs (2.12) assume that density is distributed linearly along each edge of the trapezoidal element shown on the left. If, in contrast, density is a quadratic function of z shown as smooth curve on the right, the trapezoidal segments do not conicide with the true profile leading to a noncancellation error which appears as the difference between dark and light shaded areas, which is the difference of areas left from the solid and dashed thick lines respectively. (Note that error cancels out if $z_2 = z_3$, despite the fact that there are still errors of integral approximation along each side taken separately.)

Since F_{21} and F_{43} involve points only within their respective vertical columns and, since during vertical summation of $\mathcal{J}(\rho,z)$ cancellations occur such that only the first and the last vertical fluxes are present in the resultant expression for PGF, one can rearrange the order of operation of vertical integration and horizontal differencing and evaluate P at all $\rho_{i,k}$ locations first, using

$$P_{i,k} = P_{i,N} + g\sum_{k'=k}^{N-1} \frac{\rho_{i,k'}+\rho_{i,k'+1}}{2}\,(z_{i,k'+1}-z_{i,k'})\,, \qquad (2.15)$$

then

$$\begin{aligned} -\left.\frac{\partial P}{\partial x}\right|_z &= \frac{P_{i,k}-P_{i+1,k}}{\Delta x} \\ &\quad -g\frac{\rho_{i,k}+\rho_{i+1,k}}{2}\cdot\frac{z_{i+1,k}-z_{i,k}}{\Delta x}\,. \end{aligned} \qquad (2.16)$$

This shows that density Jacobian is just a special form of straightforward discretization of σ-coordinate PGF that naturally appears to be in the form of a P derivative along a σ surface and compensating hydrostatic term, which is the product of ρ and coordinate slope[4].

In (2.15) $P_{i,N}$ is pressure in the middle of the topmost grid box, where a special formula must be used (simi-

[4] A B-grid version of (2.15)–(2.16) appears in Gerdes, 1993, which in effect brings that study into the framework discussed here.

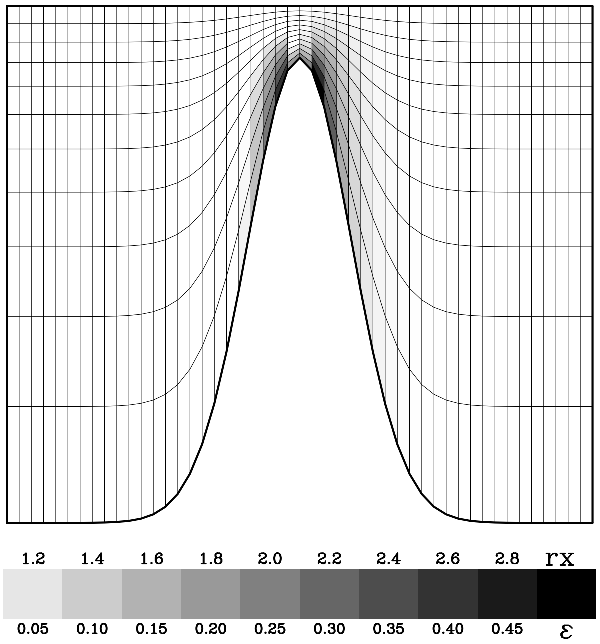

Figure 4. Vertical crossection of grid for the seamount test problem. On the left half of the plot, elements where hydrostatic consistency criterion is violated are shaded according to their value of r_x defined by (2.10), and color scheme below (with corresponging values shown above color bar). Shading on the right half of the plot shows values of geometric parameter ϵ defined by (3.3).

neither one has obvious advantage. It turns out that this is not the case, and the choice of z_* produces a significant effect in practice. To illustrate this we set up a seamount test problem and run test cases corresponding to different choices of common level according to

$$z_\gamma = (1-\gamma)z_* + \gamma z_C \,, \tag{4.1}$$

where $\gamma = \{0, 0.1, 0.2, \ldots 0.9, 1\}$; if $\gamma = 0$, the scheme is equivalent to the original Jacobian, while if $\gamma = 1$, it becomes the weighted Jacobian. The seamount problem set up is similar to that of Beckmann & Haidvogel, 1993, Chu & Fan, 1997, Mellor *et al*, 1998, and Song, 1998, with a few exceptions specified below.

The bottom topography is defined as

$$h(x,y) = D_0 - H \exp\left\{\frac{x^2+y^2}{L^2}\right\} \tag{4.2}$$

where $D_0 = 5000\,m$ is the depth far away from the seamount; $H = 4500\,m$ and $L = 40\,km$ are the seamount height and width, respectively; and the model domain is $320 \times 320\,km$ wide and has horizontal boundary conditions of periodicity in x and walls in y. An f-plane approximation is made with Coriolis frequency $10^{-4}\,s^{-1}$.

The uniform horizontal grid resolution for the base case is 48×48, implying $6.7\,km$ grid spacing. The vertical resolution for the base case is 11 non-uniformly spaced σ-levels generated by the transformation (Song & Haidvogel, 1994),

$$Z(x,y,\sigma) = \sigma h_{\min} + C(\sigma)\left(h(x,y) - h_{\min}\right) \,, \tag{4.3}$$

where

$$C(\sigma) = (1-\theta_b)\frac{\sinh(\theta\sigma)}{\sinh(\theta)} + \frac{1}{2}\theta_b\left[\frac{\tanh[\theta(\sigma+1/2)]}{\tanh(\theta/2)} - 1\right] \,,$$

$-1 \le \sigma \le 0$ is discretized uniformly, and θ and θ_b are two non-dimensional parameters controlling the vertical coordinate stretching. In all calculations performed here we use values $\theta = 3$, $\theta_b = 0$ and $h_{\min} = 500\,m$, which results in violation of hydrostatic consistency (2.10) with a maximum value

$$r_{\max} = 2.4 \tag{4.4}$$

(this is comparable to, but somewhat smaller than that used in Song, 1998, and Mellor *et al*, 1998). A vertical cross-section of the grid and distributions of r_x and geometric parameter ϵ defined by (3.3) are shown in Fig. 4. Since ϵ is well correlated with r_x, it is naturally expected that method of Song, 1998 deviates most from the original Jacobian where r_x is the largest. Fig. 4 also shows that in such places biases from equal weighting in (3.1) may be significant, especially where vertical interpolation turns into extrapolation. To examine further this correlation we note that

$$\frac{\epsilon}{r_x} = \frac{(z_4-z_3)^2 - (z_2-z_1)^2}{8\,(z_4-z_3)\,(z_2-z_1)} = \frac{\Delta z_R^2 - \Delta z_L^2}{8\Delta z_R \Delta z_L} \,, \tag{4.5}$$

where Δz_L and Δz_R are grid-box heights on the left and right sides of the trapezoidal element. In the case of a separable σ-coordinate, these two are proportional to total depth D, hence

$$\frac{\epsilon}{r_x} = \frac{D_R^2 - D_L^2}{8D_R D_L} \approx \frac{1}{2}\cdot\frac{D_R - D_L}{D_R + D_L} = \frac{1}{2}r_D \,, \tag{4.6}$$

where the approximation is valid as long as $D_R - D_L \ll D_R + D_L$. The expression on the right is recognized as the topographic-stiffness ratio (Beckmann & Haidvogel, 1993) which relates change in topography per horizontal grid point to locally averaged depth. Since this ratio proportionally decreases with increase of horizontal resolution and r_x stays the same as long as refinements of vertical and horizontal grids are proportional, one can see that ϵ decreases with grid refinement, which means that coefficients of weighted Jacobian asymptotically converge to that of the original one. This also means that in the seamount experiments, extreme values of ϵ occur on the coarsest grid and decline with refinement.

maximum baroclinic velocity,

$$|V-\langle V\rangle|_{\max}=\max\Big\{u_{i+\frac{1}{2},j,k}-\overline{u}_{i+\frac{1}{2},j}\,,\qquad v_{i,j+\frac{1}{2},k}-\overline{v}_{i,j+\frac{1}{2}}\Big\}\,. \tag{4.19}$$

(In (4.14)–(4.19) above $\Delta\mathcal{V}_{i,j,k}$, $\Delta\mathcal{V}_{i+\frac{1}{2},j,k}$, and $\Delta\mathcal{V}_{i,j+\frac{1}{2},k}$ are control volumes of ρ and velocity component grid boxes,

$$\mathcal{V}=\sum_{i,j,k}\Delta\mathcal{V}_{i,j,k} \tag{4.20}$$

is total volume of the domain,

$$\overline{u}_{i+\frac{1}{2},j}=\frac{1}{\overline{\Delta\mathcal{V}}_{i+\frac{1}{2},j}}\sum_{k=1}^{N}\Delta\mathcal{V}_{i+\frac{1}{2},j,k}u_{i+\frac{1}{2},j,k} \tag{4.21}$$
$$\overline{v}_{i,j+\frac{1}{2}}=\frac{1}{\overline{\Delta\mathcal{V}}_{i,j+\frac{1}{2}}}\sum_{k=1}^{N}\Delta\mathcal{V}_{i,j+\frac{1}{2},k}v_{i,j+\frac{1}{2},k}$$

are barotropic velocity components, and

$$\overline{\Delta\mathcal{V}}_{i+\frac{1}{2},j}=\sum_{k=1}^{N}\Delta\mathcal{V}_{i+\frac{1}{2},j,k} \tag{4.22}$$
$$\overline{\Delta\mathcal{V}}_{i,j+\frac{1}{2}}=\sum_{k=1}^{N}\Delta\mathcal{V}_{i,j+\frac{1}{2},k}$$

are barotropic control volumes.)

From our experiments we find four of these quantities, $\mathcal{E}_{\text{kin}}$, f_{bar}, $V_{\max}$, and $|V-\langle V\rangle|_{\max}$, as the most informative, Fig. 5 . Behavior of the remaining $\mathcal{E}_{\text{bar}}$ and $\langle V\rangle_{\max}$ qualitatively follow $\mathcal{E}_{\text{kin}}$ and $V_{\max}$, hence we chose not to report them. We might also report on the baroclinic part of kinetic energy,

$$\mathcal{E}_{\text{bcn}}=\frac{1}{2\mathcal{V}}\sum_{i,j,k}\Big[\Delta\mathcal{V}_{i+\frac{1}{2},j,k}\Big(u_{i+\frac{1}{2},j,k}-\overline{u}_{i+\frac{1}{2},j}\Big)^2+\Delta\mathcal{V}_{i,j+\frac{1}{2},k}\Big(v_{i,j+\frac{1}{2},k}-\overline{v}_{i,j+\frac{1}{2}}\Big)^2\Big]\,, \tag{4.23}$$

but it is redundant with (4.14) and (4.16), since $\mathcal{E}_{\text{bcn}}=\mathcal{E}_{\text{kin}}-\mathcal{E}_{\text{bar}}$.

Since ideally the fluid should remain at rest, values above zero should be interpreted as due to numerical errors, Fig. 5 leads to the following observations:

- The overall level of error after long time exceeds by at least one order of magnitude the initial hydrostatic PGF error (measured by holding the ρ field at its initial state and then running the model in a so-called diagnostic regime, resulting in velocity field geostrophically balanced with spurious PGF).

- The long-term error is predominantly barotropic, with 90% of total kinetic energy. Compared to barotropic energy, the energy of the baroclinic component (not shown) and maximum baroclinic velocity error show lesser sensitivity to the choice of z_*. Furthermore, evolution of baroclinic error shows evidence of advective compensation (Mellor *et al*, 1998), so that after initial growth it reaches a maximum and then relaxes to a smaller level. No such compensation occurs for the barotropic error measures.

- The the results show a major sensitivity to the choice of z_*, with total velocity error differences among the cases as much as factor of 4 and error kinetic energy one order of magnitude.

- $\gamma=0.5$, which corresponds to the "half-and-half" blend of standard and weighted Jacobians, clearly shows the optimum levels of error by all measures.

The first remark partially explains the fact that many attempts to introduce better PGF schemes failed to produce a practically useful result: most of the effort was spent in trying to improve accuracy of hydrostatic balance, while the error level in realistic simulations is controlled primarily by the behavior of the whole model, including not only PGF, but also tracer advection scheme, forms of diffusivity, and viscosity operators.

This might suggest that the solution to the PGF error dilemma lies in the consideration of energetic consistency, which links the design of PGF discretization with the form of advection scheme for tracers (Mesinger & Arakawa, 1976; Janjic, 1977; Arakawa & Suarez, 1983; Michailovich & Janjic, 1986; and Song & Wright, 1998[5]). This consideration appeals to the fact that in a stratified fluid ρ is redistributed predominantly by vertical velocity[6], and since vertical velocity is obtained from divergence of horizontal velocities, which in turn is controlled by the horizontal PGF, failure to obtain cancellation of potential and kinetic energy conversion terms (the "omega-alpha" terms, Janjic, 1977) for the discretized of ρ and momentum equations may cause computational instability. As the result, the discrete computation of P from ρ is linked with vertical interpolation of ρ to compute vertical advective fluxes. This relation exists in any model, including those with a

[5] Song & Wright, 1998, contains proof of energetic, momentum, and bottom torque consistency for the standard Jacobian only. No such proof is available for the weighted Jacobian.

[6] In the case of linearized momentum equations, the only mechanism for changing ρ is due to interaction of background stratification and vertical velocity. This is often the dominant mechanism in the general case too.

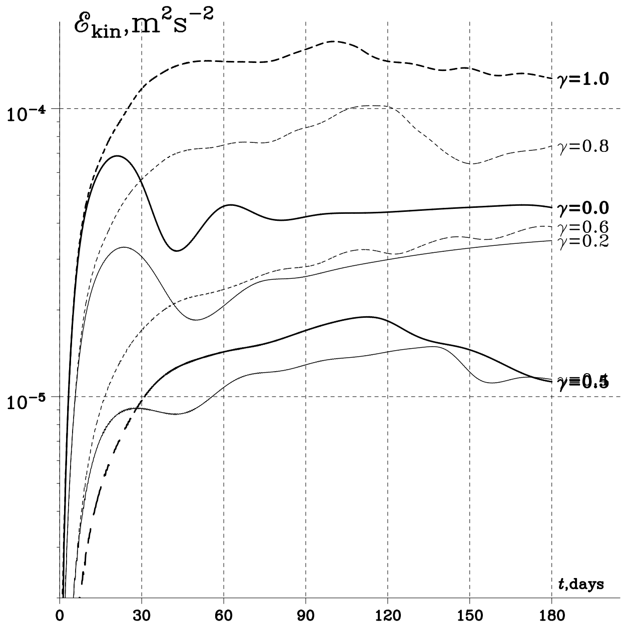

Figure 6. Time history of total energy $\mathcal{E}_{\mathrm{kin}}$ for Seamount test problem on $96 \times 96 \times 22$ grid (all conditions are the same as on Fig. 5, except the grid resolution).

z-coordinate. However, in addition to that, due to coordinate slopes in a σ-model, there is a similar link between mid-point interpolations of ρ in along-σ directions in PGF and horizontal advection schemes (cf., (A.13) in Appendix A). However, experience to date shows that in practice an energetically consistent pair of PGF and advection schemes can be easily defeated in terms of error level by an energetically non-consistent pair (e.g., Beckmann & Haidvogel, 1993, as well as experience reported here). Another difficulty here is that analytical proof of energetic consistency is possible only for relatively simple schemes for advection and PGF, and for idealized linear Equation of State of sea water.

The existence of γ corresponding to the minimal error and optimality of the half-and-half blend is very striking, especially after similar behavior was observed in different model configurations (e.g., Fig. 6, where grid resolution is doubled in comparison with Fig. 5, and $\gamma = 0.5$ still maintains its one-order-of-magnitude edge over $\gamma = 0$ or 1). After discovering this phenomenon, practical oceanic modelers did not waste any time in search for its explanation before putting it to use, making it by far the most heavily used PGF scheme in the SCRUM/ROMS[7] community. Yet, it has to be emphasized that this choice has no mathematical foundation and is purely empirical in its nature, for example there is no reason to expect that $\gamma = 0.5$ will be universally optimal for any combination of stratification, bottom topography and grid resolution.

[7] ROMS – Regional Oceanic Modeling System.

5. A Density-Jacobian with Monotonized Cubic Polynomial Fits

Sensitivity to the choice of z_* as well as consideration of alternative forms of density Jacobian lead us to a conclusion that all means to solve the σ-coordinate PGF problem, while staying within the second-order accurate methods, have been exhausted without producing a decisive result. In this section we seek an extension of the Jacobian scheme to higher orders of accuracy. As shown before, the original second-order Jacobian retains a high degree of symmetry and can be equivalently represented in several different forms. Since it is unlikely that a high-order scheme would retain all these symmetries, different versions may be derived depending which second-order prototype is used as the starting point.

We find that a particularly attractive path is to start with the *pseudo-flux* form (2.11) stemming from Green's theorem (2.14). The proposed approach is based on cubic polynomial reconstruction for z and ρ and subsequent analytical integration. Therefore, our goal is to compute

$$-\iint\limits_{\mathcal{A}} \left.\frac{\partial \rho}{\partial x}\right|_z \mathrm{d}x\,\mathrm{d}z\,, \tag{5.1}$$

where $\mathcal{A}$ is the shaded area in Fig. 7. This problem is equivalent to computation of the contour integral,

$$\begin{aligned} -\oint \rho\,\mathbf{dz} = FX_{i,k+\frac{1}{2}} + FC_{i+\frac{1}{2},k+1} \\ -FX_{i+1,k+\frac{1}{2}} - FC_{i+\frac{1}{2},k}\,, \end{aligned} \tag{5.2}$$

which consists of four segments, two along the side facets,

$$FX_{i,k+\frac{1}{2}} = \int\limits_{s_{i,k}}^{s_{i,k+1}} \rho \frac{\partial z}{\partial s}\,\mathrm{d}s\,, \tag{5.3}$$

and two along the upper and lower facets,

$$FC_{i+\frac{1}{2},k} = \int\limits_{\xi_{i,k}}^{\xi_{i+1,k}} \rho \frac{\partial z}{\partial \xi}\,\mathrm{d}\xi\,. \tag{5.4}$$

In both cases integrals are understood as line integrals and (ξ, s) are the transformed curvilinear coordinates onto which the physical coordinates (x, z) are mapped. In the case where both ρ and z are approximated by segments of linear functions, analytical integration of (5.3)–(5.4) leads to (2.11.

where

$$d_{\pm\frac{1}{2}} = \left.\frac{\partial\rho}{\partial\xi}\right|_{\xi=\pm\frac{1}{2}} \quad \text{and} \quad dz_{\pm\frac{1}{2}} = \left.\frac{\partial z}{\partial\xi}\right|_{\xi=\pm\frac{1}{2}} . \quad (5.12)$$

The terms in curly brackets in (5.11) can be interpreted as high-order correction to the trapezoidal integration rule used in (2.11). The remarkable antisymmetry of these terms stems from the property

$$\int_{-\frac{1}{2}}^{+\frac{1}{2}} \rho\frac{\partial z}{\partial\xi}\mathrm{d}\xi = \rho_{+\frac{1}{2}}z_{+\frac{1}{2}} - \rho_{-\frac{1}{2}}z_{-\frac{1}{2}} - \int_{-\frac{1}{2}}^{+\frac{1}{2}} z\frac{\partial\rho}{\partial\xi}\mathrm{d}\xi\,, \quad (5.13)$$

leading to exact antisymmetry of the discrete Jacobian,

$$\mathcal{J}(\rho,z) = -\mathcal{J}(z,\rho)\,, \quad (5.14)$$

now extended to potentially higher orders of accuracy.

The formulation of the PGF algorithm (5.2), (5.3), (5.4), and (5.11) is now complete, with the exception that application of (5.11) requires an estimate of derivatives $d_{\pm\frac{1}{2}}$ and $dz_{\pm\frac{1}{2}}$. These can be computed, for example, from the condition of continuity of the second derivatives using cubic spline formalism, which leads to a tri-diagonal problem

$$d_{j-1} + 4d_j + d_{j+1} = 3\left(f_{j+1} - f_{j-1}\right)\,, \quad (5.15)$$

where $j = 1, \dots, N$ is either horizontal or vertical grid index. This results in a compact fourth-order interpolation, which is generally more accurate than conventional finite-difference methods (McCalpin, 1994, Chu & Fan, 1997) as long as the interpolated fields are sufficiently smooth on the grid, but, as we will soon demonstrate, it is prone to oscillations and is not robust if there are sudden changes in gradient of the field from one grid interval to the next. In the simplest case derivatives $d_{+\frac{1}{2}}$ are estimated as finite differences,

$$d_{+\frac{1}{2}} = \frac{f_{+\frac{3}{2}} - f_{-\frac{1}{2}}}{2} = \frac{\Delta^+ + \Delta^-}{2}\,, \quad (5.16)$$

where

$$\Delta^- = f_{+\frac{1}{2}} - f_{-\frac{1}{2}} \quad \text{and} \quad \Delta^+ = f_{+\frac{3}{2}} - f_{-\frac{1}{2}} \quad (5.17)$$

are the elementary differences on the left and right sides from point $f_{+\frac{1}{2}}$. Substitution of (5.16) into (5.8) leads to the same expressions for $f^{(0)}$ and $f^{(2)}$ as in (5.6), and consequently the same integral approximation (5.7). However, $f^{(1)}$ and $f^{(3)}$ are different; moreover, $f^{(1)}$ in (5.8) using (5.16) approximates the first derivative with only second-order accuracy, while $f^{(3)}$ is off by a factor of 3 in comparison with the corresponding value from (5.6). Although the polynomial fit defined by (5.5)–(5.16) already produces fourth-order accuracy, it has the disadvantage of producing spurious oscillations if the grid values are not smooth.

If alternatively to (5.16) we define

$$d_{+\frac{1}{2}} = 2\bigg/\left[\frac{1}{\Delta^+} + \frac{1}{\Delta^-}\right] = \frac{2\Delta^+\Delta^-}{\Delta^+ + \Delta^-}\,, \quad (5.18)$$

as long as Δ^+ and Δ^- have the same sign, and

$$d_{+\frac{1}{2}} = 0\,, \quad (5.19)$$

if $\Delta^+\Delta^- \le 0$, then it is guaranteed that both $d_{+\frac{1}{2}}$ and $d_{-\frac{1}{2}}$ have the same sign as $f_{+\frac{1}{2}} - f_{-\frac{1}{2}}$, and

$$\begin{aligned} \left|d_{+\frac{1}{2}}\right| &< 2\cdot\min\left\{\left|f_{+\frac{1}{2}} - f_{-\frac{1}{2}}\right|\,,\,\left|f_{+\frac{3}{2}} - f_{+\frac{1}{2}}\right|\right\} \\ \left|d_{-\frac{1}{2}}\right| &< 2\cdot\min\left\{\left|f_{+\frac{1}{2}} - f_{-\frac{1}{2}}\right|\,,\,\left|f_{-\frac{1}{2}} - f_{-\frac{3}{2}}\right|\right\} \end{aligned} \quad (5.20)$$

i.e., at least no more than $2\left|f_{+\frac{1}{2}} - f_{-\frac{1}{2}}\right|$ in both cases, which is sufficient to prove that the first derivative of cubic polynomial fit (5.5)–(5.8),

$$\frac{\partial f}{\partial\xi} = f^{(1)} + f^{(2)}\xi + \frac{f^{(3)}\xi^2}{2} \quad (5.21)$$

maintains its sign to be the same as $f_{+\frac{1}{2}} - f_{-\frac{1}{2}}$ throughout the whole interval of ξ within its area of definition,

$$\left(f_{+\frac{1}{2}} - f_{-\frac{1}{2}}\right)\frac{\partial f}{\partial\xi} \ge 0 \qquad \forall\xi: \quad -\frac{1}{2} \le \xi \le +\frac{1}{2}\,. \quad (5.22)$$

In its turn, it guarantees that

$$\left.\begin{array}{c} f_{-\frac{1}{2}} \le f(\xi) \le f_{+\frac{1}{2}} \\ \text{or} \\ f_{-\frac{1}{2}} \ge f(\xi) \ge f_{+\frac{1}{2}} \end{array}\right\}\ \forall\xi: \quad -\frac{1}{2} \le \xi \le +\frac{1}{2}\,, \quad (5.23)$$

regardless of the values $f_{-\frac{3}{2}}$ and $f_{+\frac{3}{2}}$ at the extreme points of the stencil.

Another advantage of (5.18) over (5.16) is its ability to "absorb" nonuniformity of the grid without loss of accuracy in a manner described in Treguier, *et al*, 1996. Suppose that discretized field $\{\rho_k\,, k = 1, N\}$ is defined at locations $\{\rho_k\,, k = 1, N\}$, such that $\Delta z_{k+\frac{1}{2}} \equiv z_{k+1} - z_k \ne \Delta z_{k-\frac{1}{2}} \equiv z_k - z_{k-1}$. Then the second-order accurate approximation for $\partial\rho/\partial z$ at location k is

$$\left.\frac{\partial\rho}{\partial z}\right|_{z=z_k} = \frac{\Delta z_{k-\frac{1}{2}}\frac{\rho_{k+1}-\rho_k}{\Delta z_{k+\frac{1}{2}}} + \Delta z_{k+\frac{1}{2}}\frac{\rho_k-\rho_{k-1}}{\Delta z_{k-\frac{1}{2}}}}{\Delta z_{k+\frac{1}{2}} + \Delta z_{k-\frac{1}{2}}}\,, \quad (5.24)$$

which is derived by assuming a parabolic fit for $\rho = \rho(z)$ (such that it produces exact values of ρ_{k-1}, ρ_k and ρ_{k+1}

- Linear extrapolation: $\partial^2 f/\partial s^2 = 0$ at locations of f_N and f_1),

$$d_N = \frac{3}{2}\left(f_N - f_{N-1}\right) - \frac{1}{2}d_{N-1} \qquad (5.36)$$

$$d_1 = \frac{3}{2}\left(f_2 - f_1\right) - \frac{1}{2}d_2\,, \qquad (5.37)$$

where we have assumed that all quantities on the r.h.s. are known.

The use of (5.34)–(5.35) is justified only if Neumann boundary conditions are physically justified; otherwise, the use of (5.34)–(5.35) can be interpreted as formal reduction of order of accuracy (to the first order) near the boundary. Similarly, (5.36)–(5.37) is equivalent to assumption of a linear distribution of the interpolated field within the grid box adjacent to the boundary, which is formally second-order accurate. In principle, formally more accurate extrapolation formulas can be derived; however, according to our practical experience, going beyond second-order accuracy near the boundary makes the resultant algorithm extremely non-robust in the case of coarse resolution. Note that harmonic averaging (5.18) guarantees that

$$|d_{N-1}| < 2\,|f_N - f_{N-1}|\ , \qquad (5.38)$$

and that d_{N-1} has the same sign as $f_N - f_{N-1}$. Therefore (5.36) guarantees that (i) d_N always maintains the same sign as both $f_N - f_{N-1}$ and d_{N-1}, and (ii) d_N does not exceed $\frac{3}{2}\left(f_N - f_{N-1}\right)$, regardless of non-smoothness of grid data within the three points adjacent to the boundary.

Fig. 8 compares density profiles $\rho(z)$ reconstructed by the three interpolation methods discussed here for the case of step-like profile. As expected, on a hydrostatically inconsistent grid, interpolation along σ-slope results in greater vertical distances between grid points (Fig. 8, second column), making it more difficult for the interpolation scheme. As the result, spline and algebraic averaging tend to oscillate, while harmonic averaging produces a robust (though not very accurate) monotonic profile.

Density-Jacobian Algorithm

We summarize the proposed algorithm[8] as the following sequence:

- Compute and store in provisional arrays elementary vertical differences of $\Delta\rho_{i,k+\frac{1}{2}} = \rho_{i,k+1} - \rho_{i,k}$ and $\Delta z_{i,k+\frac{1}{2}} = z_{i,k+1} - z_{i,k}$ for all $k = 1, \ldots, N-1$.

[8]This algorithm is known as `prsgrd32.F` in the ROMS code.

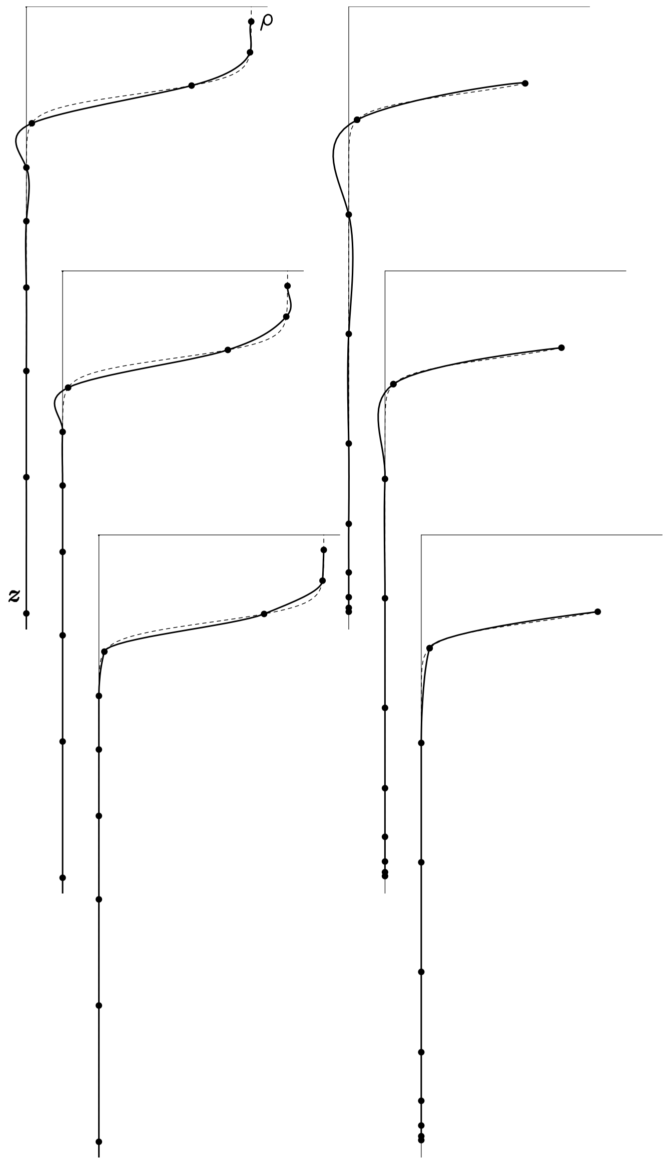

Figure 8. Comparison of three interpolation methods for a step-like profile: **upper row** — both z and ρ are interpolated as functions of s or ξ using cubic spline (5.15); black dots correspond to the actual data points; solid curves represent interpolated profiles, and dashed — the exact profiles. **middle row** — local cubic polynomial based on algebraic averaging of elementary differences (5.16). **bottom row** — using harmonic averaging (5.18). **Left column** — interpolation in vertical direction; **right column** — interpolation along σ-slope across the location of extreme r_x on Fig. 4 resulting in a more concentrated placement of points near the bottom, where σ-surfaces tend to be more horizontal, but effectively coarser resolution near the thermocline; the uppermost data pont on the profile corresponds to the horizontal location above the top of Seamount.

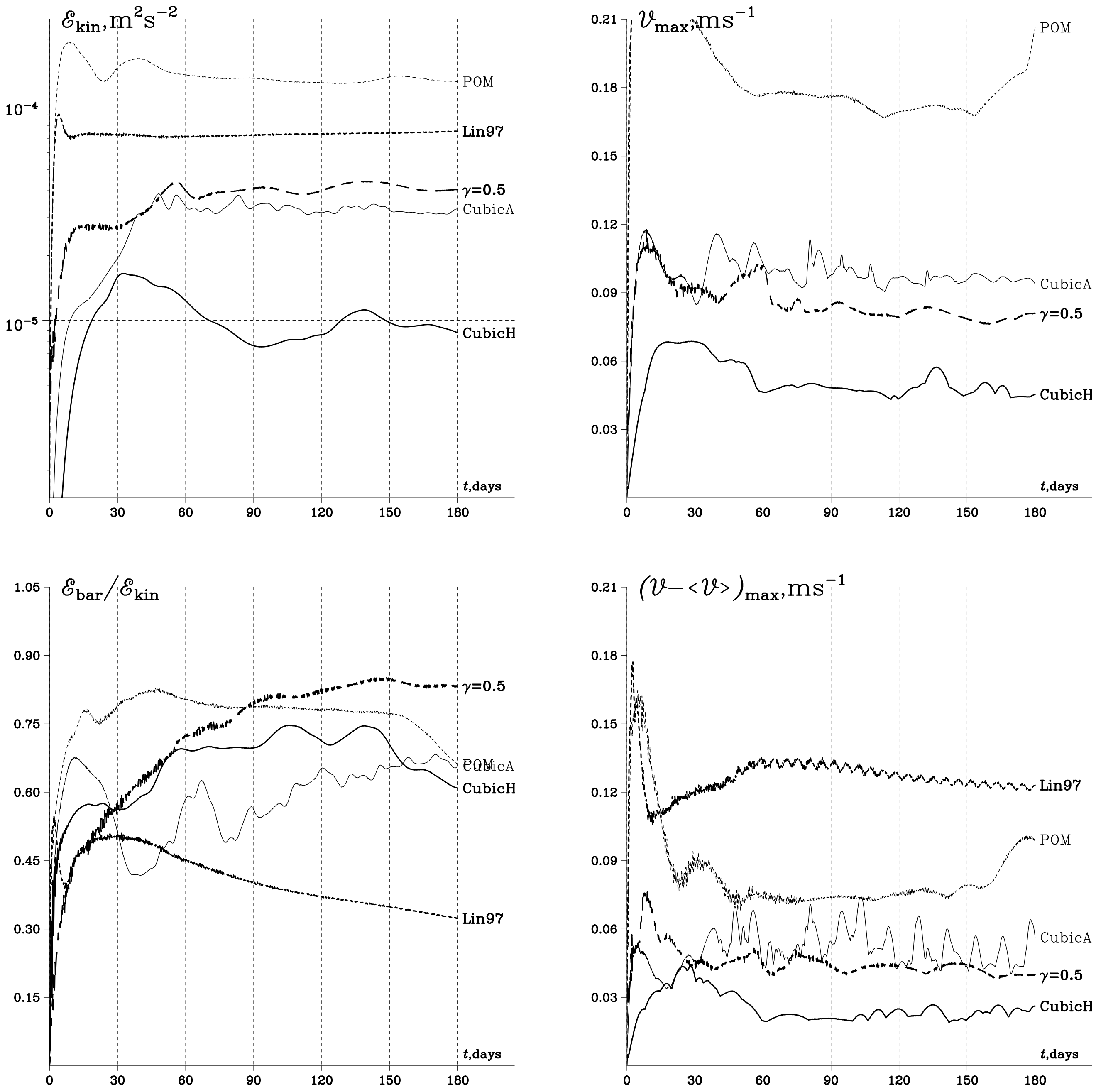

Figure 9. Same as Fig. 5, but for a different set of pressure-gradient schemes. *Cubic H* – method described in the previous section using (5.11) as integration rule with harmonic averaging of elementary slopes by (5.18); *Cubic A* – the same as *Cubic H*, but harmonic averaging is replaced with algebraic mean (5.16); *POM* – POM scheme (same as $\gamma = 0$); $\gamma = 0.5$ – optimum "half-and-half" blend of standard and weighted Jacobians; *Lin97* – Lin's, 1997 finite-volume method (pressure Jacobian scheme). Note that maximum velocity error $V_{\rm max}$ is outside the plotted range for *Lin97*.

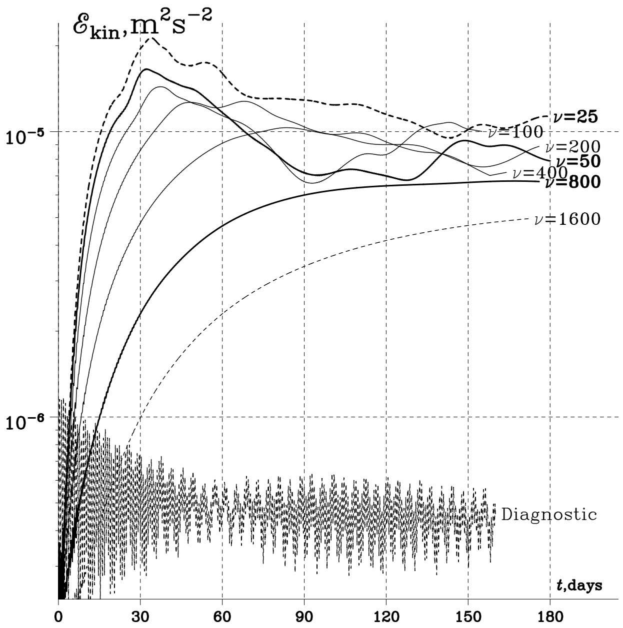

Figure 10. Sensitivity of $\mathcal{E}_{\rm kin}$ to viscosity. Labels $\nu = 25, 50, \dots, 1600$ at the end of each curve indicate value of viscosity in m^2/s. *Diagnostic* – in this test run density field was kept constant, resulting in flow geostrophically balanced with spurious pressure gradient. This error level provides comparative measure of the error in hydrostatic balance for the initial density field. Grid resolution is $48 \times 48 \times 11$.

have the opposite sign to the difference of the nearest adjacent grid-point values. Taking into account the compressibility of seawater causes difficulty because the only physically meaningful principle of monotonicity here is positive gravitational stability of a stratified fluid, which is not equivalent to maintaining the sign of the derivative of the reconstructed *in situ* ρ profile.

The Equation of State (EOS) for seawater, e.g., Millero *et al*, 1980, is usually written as

$$\rho = \rho(T, S, P)\,, \tag{7.2}$$

where ρ, T, S and P are *in situ* density, temperature, salinity, and pressure respectively. This equation was reformulated by Mellor 1991, Jackett & McDougall, 1995, to allow input of potential temperature, salinity, and depth instead of P,

$$\rho = \rho(\theta, S, z)\,, \tag{7.3}$$

which is more suitable for use in oceanic models because potential temperature (not *in situ* temperature) and salinity are the advectively conserved quantities. Replacement of *in situ* P by depth effectively neglects the effects of baroclinicity due to compressibility in computation of ρ by replacing $g\int \rho dz$ with $g\rho_0 z$. The resultant difference is formally within the accuracy of the Boussinesq approximation and is acceptably small for any realistic oceanographic situation. In the case of an incompressible EOS,

$$\rho = \rho(\theta, S)\,, \tag{7.4}$$

the monotonicity constraint of the reconstruction algorithm guarantees that if all differences,

$$\rho_k - \rho_{k+1} \equiv \rho\left(\theta_k, S_k\right) - \rho\left(\theta_{k+1}, S_{k+1}\right) > 0\,, \qquad k = 1, \dots, N{-}1 \tag{7.5}$$

are positive, then the reconstructed profile is also everywhere positively stratified. This can no longer be guaranteed if EOS includes compressibility. The discretized (7.3) is

$$\rho_k = \rho\left(\theta_k, S_k, z_k\right) \quad k = 1, \dots, N\,, \tag{7.6}$$

while the compressible analog of the stability condition (7.5) translates into

$$\rho\left(\theta_k, S_k, z_{k+\frac{1}{2}}\right) - \rho\left(\theta_{k+1}, S_{k+1}, z_{k+\frac{1}{2}}\right) > 0\,, \qquad k = 1, \dots, N{-}1\,, \tag{7.7}$$

where differencing is performed in an adiabatic fashion, since $\rho\left(\theta_k, S_k, z_{k+\frac{1}{2}}\right)$ and $\rho\left(\theta_{k+1}, S_{k+1}, z_{k+\frac{1}{2}}\right)$ are brought to the common level of $z_{k+\frac{1}{2}}$, which in the simplest case is equal to $\frac{1}{2}\left(z_k + z_{k+1}\right)$. Because of this feature (7.7) is not equivalent to just

$$\rho_k - \rho_{k+1} > 0\,, \quad k = 1, \dots, N{-}1 \tag{7.8}$$

where ρ_k are computed by (7.6). In fact, because of compressibility,

$$\rho_k - \rho_{k+1} \;>\; \rho\left(\theta_k, S_k, z_{k+\frac{1}{2}}\right) - \rho\left(\theta_{k+1}, S_{k+1}, z_{k+\frac{1}{2}}\right)\,,$$

there is the possibility that the r.h.s. can become negative while the l.h.s. remains positive.

To address this problem we decompose the EOS (cf., Jackett & McDougall, 1995),

$$\rho = \frac{\rho_1(\theta, S)}{1 + z/K(\theta, S, z)}\,, \tag{7.9}$$

where $\rho_1(\theta, S)$ is the density at the pressure of 1 atmosphere (i.e., $z = 0$) and $K(\theta, S, z)$ is the bulk secant modulus, which takes compressibility into account. Both $\rho_1(\theta, S)$ and $K(\theta, S, z)$ are approximated by polynomial fits of θ, S, $S^{1/2}$, and z. Furthermore, (7.9) may be rewritten as

$$\rho = \frac{\rho_0 + \rho_1'(\theta, S)}{1 + z/\left(K_0 + K'(\theta, S, z)\right)}\,, \tag{7.10}$$

to the choice of reference level z_* (see (4.1), nor do we see any significant growth of energy of the barotropic mode.

To cure this problem, one must somehow exclude the large terms in (7.11), which are functions of z only, cf., Mellor *et al*, 1994, Dukowicz, 2001. Thus, within the accuracy of the Boussinesq approximation and for the purpose of PGF computation, we therefore can use a simplified equation of state,

$$\rho = \rho_1'(\theta, S) + \frac{\rho_0 K'(\theta, S, z) \cdot z}{K_0^2}\,, \qquad (7.12)$$

which still retains a nonlinear dependency of ρ on T and S. Alternatively, one may subtract

$$\rho_{\rm bak}(z) = \frac{\rho_0}{1 + z/K_0} \qquad (7.13)$$

from (7.10), which, after cancellation of all large terms yields,

$$\rho = \frac{\rho_1'\,(K_0 + K')\,(K_0 + z) + \rho_0 K' \cdot z}{(K_0 + K' + z)\,(K_0 + z)}\,, \qquad (7.14)$$

which can be used as an alternative to (7.10) without any EOS approximation at all. Furthermore, one can absorb further leading terms depending only from z into K_0 in (7.13), $K_0 = K_0^{(0)} + K_0^{(1)} z + K_0^{(2)} z^2$, which produces an even more accurate cancellation of the vertical ρ gradient due solely to compressibility.

A ρ field computed by (7.12) or (7.14) can be considered to be the dynamically relevant density, since it retains only terms which have a nontrivial contribution to the PGF. In both cases an effort has been made to remove the dominant terms which cause the distinction between adiabatic (7.7) and *in situ* (7.8) ρ gradients, and therefore they are more appropriate for use in a monotonicity-preserving reconstruction algorithm. To demonstrate the practical consequences of replacing (7.10) with (7.12) and (7.14), we compute ρ using the realistic data shown on the left in Fig. 12 using incompressible EOS (7.4) and three different versions for treatment of compressibility, (7.9), 7.12), and (7.14). In this example the vertical gradient of *in situ* ρ is at least one order of magnitude greater than the adiabatic gradient below z=500 m depth. Although reasonably close in the upper 500 m, vertical derivatives of the newly introduced quantities may differ significantly from the desired adiabatic derivative in the abyssal part and may even have a different sign, which makes them unsuitable for the use in a monotonicity-preserving reconstruction algorithm[10].

The fundamental limitation of the techniques described thus far is that they rely upon additive cancellation of errors by subtracting an *a priori* chosen function of z from ρ, which is assumed to be close enough to the actual *in situ* ρ. Hence, errors may be reduced significantly but not eliminated completely, and the whole approach remains too sensitive to the choice of global parameters such as ρ_0, K_0 (which implicitly depend on globally chosen reference values for potential temperature and salinity). We therefore are motivated to develop a new EOS representation which does not rely on such cancellation. To do this, we first note that

$$\left.\frac{\partial\rho\,(\theta,S,z)}{\partial x}\right|_z = \left.\frac{\partial\rho}{\partial\theta}\right|_{S,z} \left.\frac{\partial\theta}{\partial x}\right|_z + \left.\frac{\partial\rho}{\partial S}\right|_{\theta,z} \left.\frac{\partial S}{\partial x}\right|_z\,, \qquad (7.15)$$

which translates into

$$\mathcal{J}\,(\rho, z) = -\alpha \mathcal{J}\,(\theta, z) + \beta \mathcal{J}\,(S, z)\ , \qquad (7.16)$$

where

$$\alpha\,(\theta, S, P) = -\left.\frac{\partial\rho}{\partial\theta}\right|_{S,P} \qquad \beta\,(\theta, S, P) = +\left.\frac{\partial\rho}{\partial S}\right|_{\theta,P} \qquad (7.17)$$

are thermal expansion and saline contraction coefficients defined (by EOS) in the usual thermodynamical sense, and $P = g\rho_0 z$ is hydrostatic pressure. Eq. (7.16) has an advantage over computing *in situ* ρ via EOS and then using it to compute $\mathcal{J}\,(\rho, z)$ because the nonlinearity of EOS (associated with nonlinear θ- and S-dependency as well as with compressibility) no longer contributes to errors of hydrostatic balance in the discretized Jacobian. Eq. (7.16) generates no erroneous flow if θ and S are spatially uniform (e.g., as in Fig. 11.

The remaining problem with (7.16) is the fact that it does not prevent spurious oscillations of the interpolated potential density, even if a non-oscillatory algorithm is used to interpolate θ and S[11]. And it almost doubles the computational cost, because two Jacobians are required. To address the first issue and to mitigate the cost, we note that the flux-difference algorithm (2.11) along with a cubic polynomial fit (5.11) and harmonic averaging (5.18) can be expressed entirely in terms of elementary differences of ρ,

$$d_{i,k+\frac{1}{2}} = \rho_{i,k+1} - \rho_{i,k} \qquad (7.18)$$

and similar differences of ρ values adjacent in the horizontal (along-σ, with indices $i+1, k$ and i, k) and diagonal

[10] The fact that it is impossible to define a field whose spatial derivatives are equivalent to adiabatic derivatives of *in situ* ρ (i.e., a globally defined potential density) is discussed in Jackett & McDougall, 1995. They show that "potential density" may be defined only locally in the context of adiabatic differentiation.

[11] This may occur, for example, if gradients of θ and S tend to cancel each other in the sense of $\alpha\nabla\theta - \beta\nabla S \approx 0$, so that a non-oscillatory interpolation algorithm applied to θ and S separately does not "feel" the non-smoothness of potential density field in a situation where consecutive differences are much larger for θ and S than for potential density.

hence,

$$\mathcal{J}\left(\rho\left(\theta,S,z\right),\,z\right)=\mathcal{J}\left(\rho_1'\left(\theta,S\right),\,z\right) \qquad (7.22)$$
$$+\sum_{n=1}^{n_{\max}} z^n\cdot\mathcal{J}\left(q_n\left(\theta,S\right),\,z\right),$$

which can be used as an alternative to (7.16) or to the straightforward computation of PGF from *in situ* ρ. On the other hand,

$$z^n\cdot\mathcal{J}\left(q_n,z\right)=\mathcal{J}\left(q_n,\frac{z^{n+1}}{n+1}\right), \qquad (7.23)$$

so instead of first computing *in situ* ρ [or any substitute quantity for it in the framework of (7.12)–(7.14)] and then using it for computation of horizontal ρ gradient, we can directly compute the contribution from each individual q_n term in $\mathcal{J}\left(\rho(\theta,S,z),\,z\right)$.

A remarkable consequence of (7.23) in the case $n=1$ is that a linear combination of discrete Jacobians,

$$\mathcal{J}\left(q_1 z,z\right)=\frac{1}{3}\left\{\mathcal{J}\left(q_1 z,z\right)+\mathcal{J}\left(q_1,z^2\right)\right\}, \qquad (7.24)$$

vanishes identically if q_1 itself is a linear function of z, even if both Jacobians in the r.h.s. fail to vanish if taken separately. This leads to a replacement of pseudo-fluxes (2.12) with[12]

$$F'''=\left\{\frac{\rho_1''+\rho_1'}{2}+q_1''\frac{2z''+z'}{6}+q_1'\frac{z''+2z'}{6}\right\}\left(z''-z'\right),$$

where prime and double prime stand for the corresponding pairs of indices 21, 42, 43, and 31 in (2.12). The resulting scheme produces no PGF error, not only if ρ is a linear function of z (as in the case of second-order Jacobian), but also if q_1 is linear in z, hence *in situ* density $\rho_1+q_1 z$ is quadratic in z, even though we use the same 2×2-point stencil of the second-order scheme. This property is especially valuable since most of the PGF errors associated with compressibility occur in the abyss, where one cannot rely solely on the order of accuracy of the PGF scheme because the vertical resolution is typically quite coarse there.

We now describe modifications to the Cubic H algorithm in the case of compressible EOS (7.20) that prevent spurious negative stratification due to oscillation of cubic polynomial fits for ρ. For the sake of simplicity and computational efficiency we restrict ourselves to the choice of $n_{\max}=1$.[13] To illustrate the practical accuracy of of this choice, we note that the adiabatic derivative of (7.20) (cf., (7.7)) with respect to transformed coordinate s (similarly ξ) is

$$\left.\frac{\partial\rho\left(\theta,S,z\right)}{\partial s}\right|_{ad}=\frac{\partial\rho_1'\left(\theta,S\right)}{\partial s}+\sum_{n=1}^{n_{\max}} z^n\frac{\partial q_n\left(\theta,S\right)}{\partial s}, \qquad (7.25)$$

where the contribution of all terms under summation is expected to be much smaller than the leading term on the r.h.s.. This is manifested by the fact that these terms are responsible for the difference between the thick and thin solid lines in the right panel of Fig. 12, and these two lines are very close to each other. This leads to the approximation of adiabatic differences (7.19) with

$$d^{(\mathrm{ad})}_{i,k+\frac{1}{2}}={\rho'_1}_{i,k+1}-{\rho'_1}_{i,k}+\frac{z_{i,k+1}+z_{i,k}}{2}\left({q_1}_{i,k+1}-{q_1}_{i,k}\right)$$

which in turn can be used to estimate *in situ* ρ derivatives at the non-staggered locations,

$$\left.\frac{\partial\rho}{\partial s}\right|_{i,k}=\frac{2d^{(\mathrm{ad})}_{i,k+\frac{1}{2}}\cdot d^{(\mathrm{ad})}_{i,k-\frac{1}{2}}}{d^{(\mathrm{ad})}_{i,k+\frac{1}{2}}+d^{(\mathrm{ad})}_{i,k-\frac{1}{2}}}+{q_1}_{i,k}\left.\frac{\partial z}{\partial s}\right|_{i,k}, \qquad (7.26)$$

which are needed by (5.11) in order to compute pseudo-fluxes using cubic polynomial fits. The first r.h.s. term is harmonically averaged adiabatic differences of ρ. As in the case of (5.18)–(5.19), this term is reset to zero if $d^{(\mathrm{ad})}_{i,k+\frac{1}{2}}$ and $d^{(\mathrm{ad})}_{i,k-\frac{1}{2}}$ have opposite signs. Since the same harmonic averaging algorithm is used for both vertical and horizontal (along σ) directions, different signs may occur even if the stratification is positive everywhere. (The expressions for adiabatic differences in the horizontal direction are exactly the same as the vertical ones, except that the index i gets increments ±1, while the index k is kept constant.) The second term in the r.h.s. of (7.26) is proportional to the gradient of ρ caused by compressibility and P changes in a neutrally stratified fluid. This adiabatic gradient separates positive and negative stratification, so that replacing the harmonic averaging (5.18) with (7.26)

[12] An identical result may be obtained by analytical integration of quadratic fit $\left[q'\left(z''-z\right)+q''\left(z-z'\right)\right]z/\left(z''-z'\right)$ over the interval from z' to z''.

[13] The method described here can easily be generalized to the case of $n_{\max}>1$ in EOS (7.20) by computing elementary adiabatic differences and the compressible term in (7.26) via

$$d^{(\mathrm{ad})}_{i,k+\frac{1}{2}}={\rho'_1}_{i,k+1}-{\rho'_1}_{i,k}+\sum_{n=1}^{n_{\max}}\left({q_n}_{i,k+1}-{q_n}_{i,k}\right)\times\frac{{z_{i,k+1}}^n+{z_{i,k}}^n}{2}$$

and

$$d^{(0)}_{i,j}=\sum_{n=1}^{n_{\max}}{q_n}_{i,k}\cdot n z^{n-1}_{i,k}\left.\frac{\partial z}{\partial s}\right|_{i,k}.$$

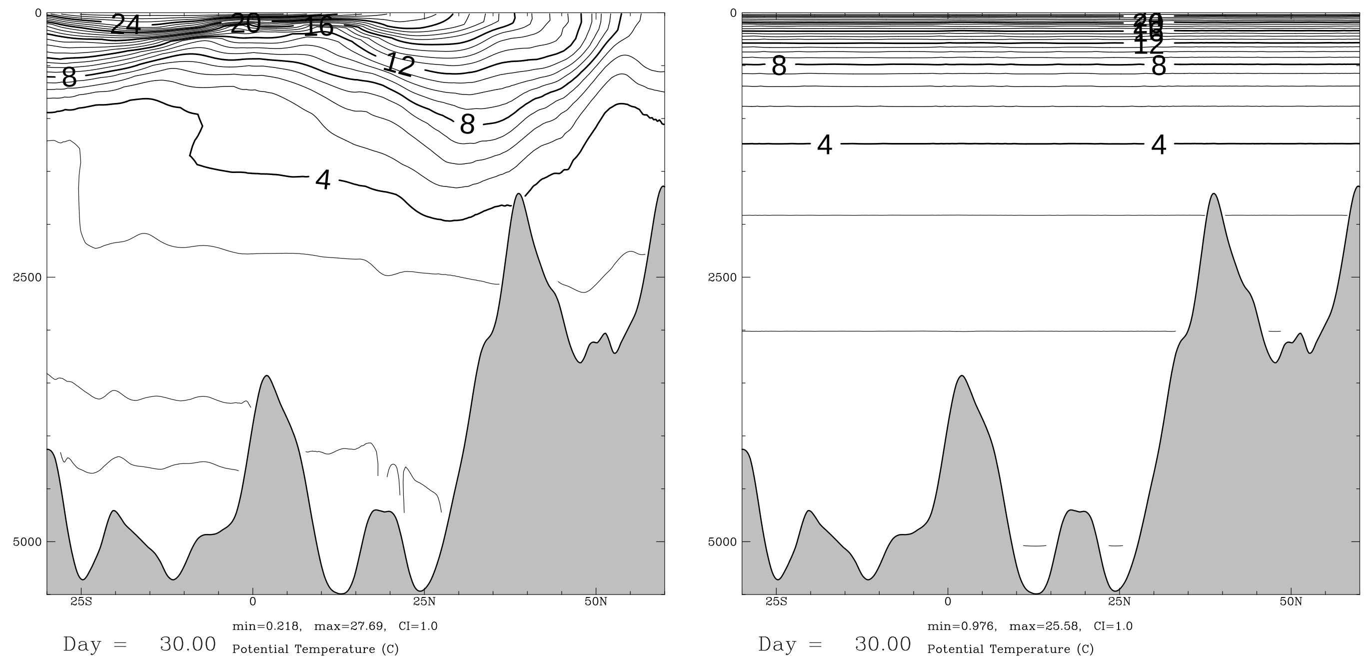

Figure 14. Potential temperature cross-section at 30^0W: **left** – from Levitus data; **right** – profile (8.1) for flat stratification tests. In both cases the contour interval is 1^0C.

ported in Haidvogel *et al*, 2000.) A comparison of our idealized profile with measurements is shown on Fig. 14. Note that our profile has comparable abyssal stratification, thermocline depth, and steepness of transition from the abyss to the thermocline. The advection scheme for material tracers is 4th-order, centered, and with harmonic averaging of elementary differences—similar to that for the Seamount problem. There is no material diffusion of any kind, neither vertical, horizontal, nor implicit via upstream-biased advection. A 4th-order centered scheme is used for momentum advection. The horizontal viscosity is 500 m^2/s.

The flow pattern after a 60-day spin up using POM Jacobian ($\gamma = 0$) and realistic EOS with compressibility turned OFF is shown in the top-left panel of Fig. 15. We find that the maximum errors for this test problem (as well the other tests reported later) occur between depths of 1000 to 1500 meters, so we choose 1500 meters as the representative level to display. The error pattern on the top-left panel is typical for σ-models. It is characterized by spurious flow along topographic slopes especially near the Equator. The error is around 3 cm/s near the Gulf-Stream area and off the North-American coast. We see a visualized mid-Atlantic ridge, closed circulation in the Caribbean abyss, and strong jets along the Equator. The largest errors occur off the Brazilian coast near Equator, 15 cm/s, which is not surprising, since stronger currents are required to achieve geostrophic balance with a given spurious PGF at lower latitudes. The weighted $\gamma = 0.5$ scheme produces comparable, but approximately 40% larger, currents and an overall similar error pattern in this test (Fig. 15, top right). Remarkably, the direction of spurious currents is reversed in comparison with the $\gamma = 0$ results. Varying the weighting factor reveals an optimal choice of $\gamma = 0.21$ for minimum mean error. This is similar to the Seamount problem experiments, except that here the optimal value is different, indicating that there is no universally optimal choice. Finally, the Cubic H scheme (Fig. 15, lower left) results in a dramatic decrease of errors and an overall change in the error pattern. It is no longer possible to see coherent currents along topographic slopes and mid-Atlantic ridge. The largest errors still occur near Equator, but now the flow pattern there has a more random character.

Turning compressibility back ON causes a dramatic increase of errors almost everywhere, which is manifested by appearance of currents along topographic slopes (Fig. 16 , top left). Although still, with somewhat smaller amplitude, the compressible Cubic H errors are more comparable with that for the second-order $\gamma = 0$ and $\gamma = 0.5$ schemes, rather than for the Cubic H case shown in the previous incompressible Fig. 15. Again, the most significant errors occur near the Equator. There is no advective compensation mechanism for PGF errors generated by a vertical ρ profile due to compressibility of seawater with uniform θ, S. Consequently, this kind of error may

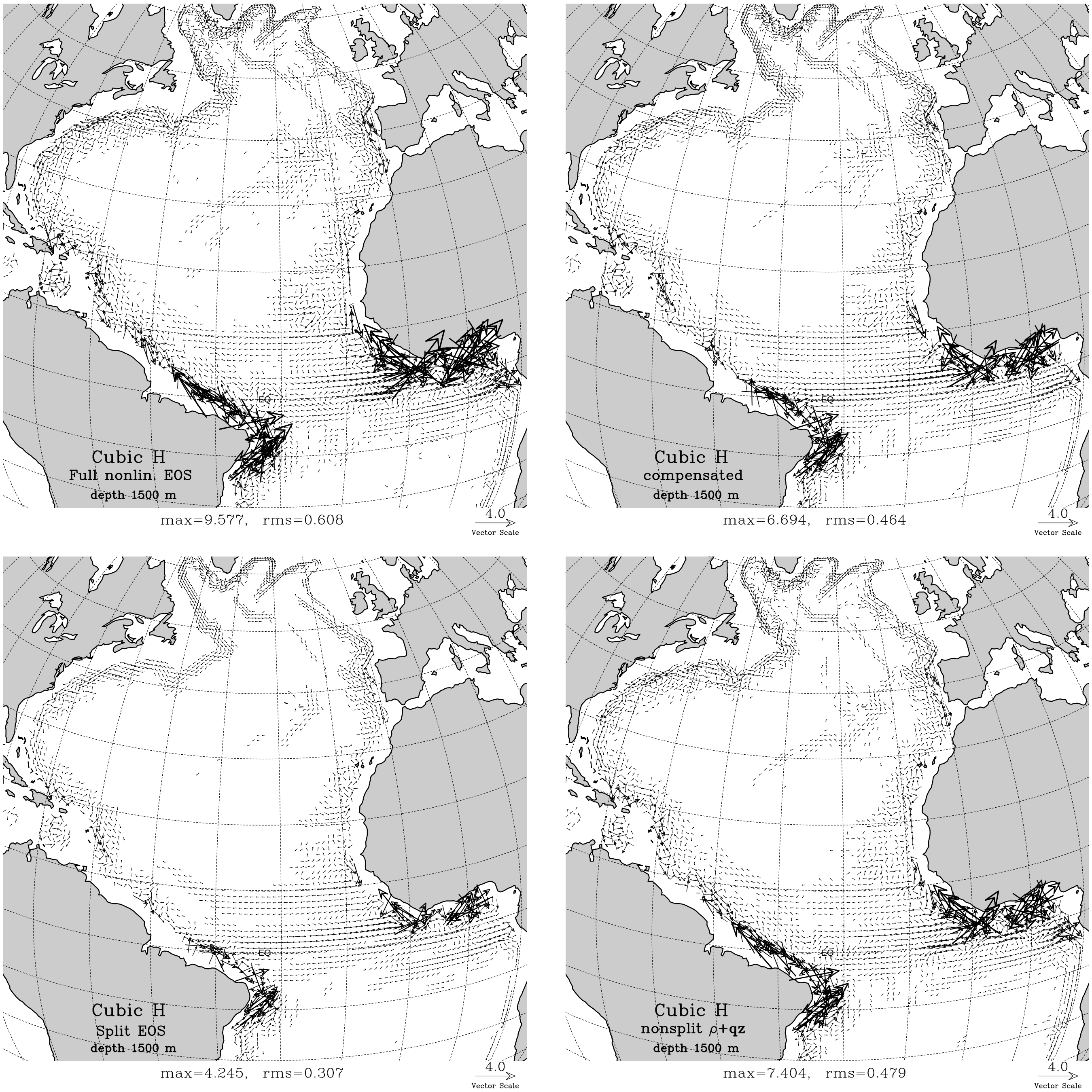

Figure 16. The same as on Fig. 15, except that now *Cubic H* – family algorithms are used in combination with different treatment of compressibility: **lop-left** – EOS (7.9) retaining all nonlinear compressibility terms; **top-right** – same as on the left, but most of the passive vertical density gradient is removed by subtracting $\rho_0/\left(1-0.1|z|/K_{00}\right)$ resulting in (7.14); **lower-left** – modified *Cubic H* algorithm in combination with EOS split into incompressible and compressible parts $\rho = \rho_1\left(\theta,S,z\right) + q_1\left(\theta,S,z\right)|z|$, thus allowing computation of derivative of density via harmonic averaging of adiabatic differences (7.26); **lower-right** – control experiment where EOS is the same as on the left, but ρ_1 and q_1 terms are combined at the stage of computation of *in-situ* density, which is then used in the original non-split version of *Cubic H*. This is equivalent to just linearization of compressibility effects.

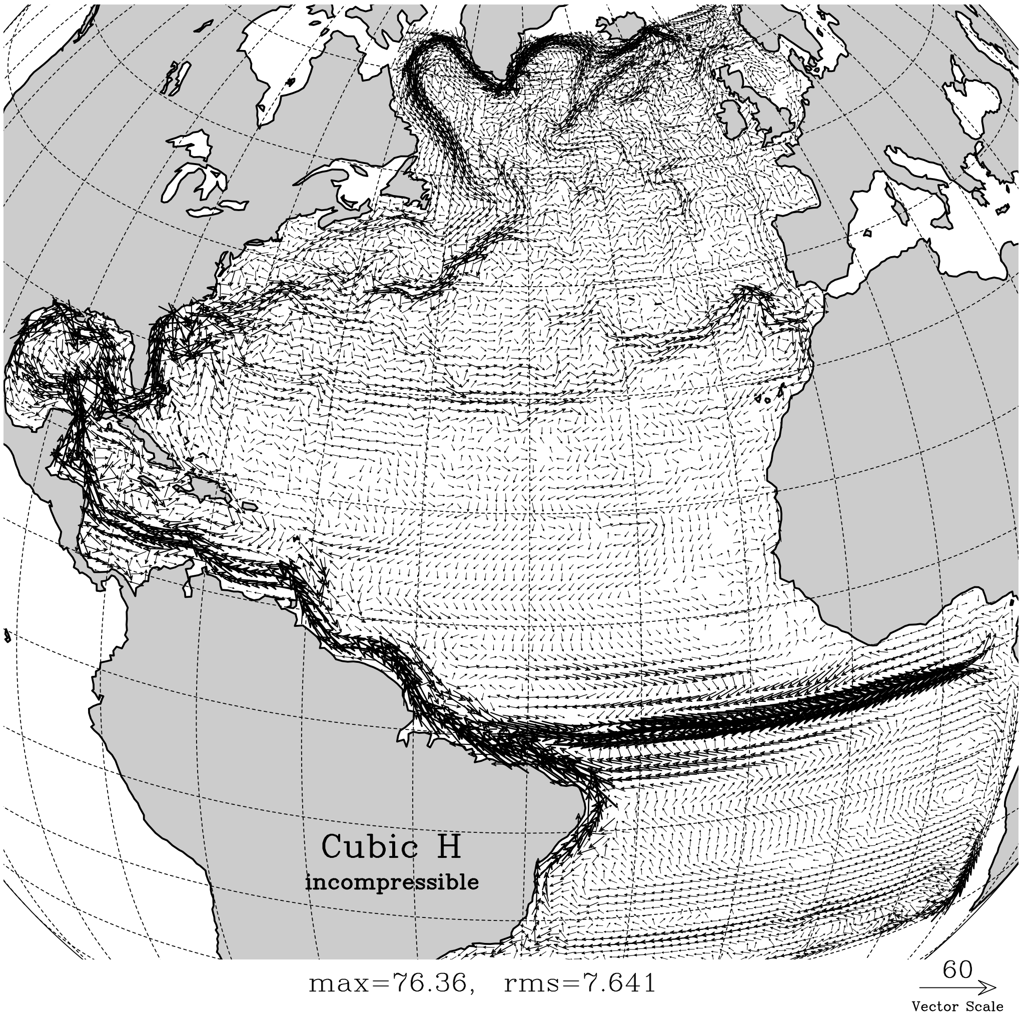

Continuation of Fig. on the previous page: now compressibility terms are turned OFF. Although qualitatively similar in its main features, energetics and maximum values of velocity to the case shown on the left, this solution is characterized by approximately 40% weaker, and prematurely separating, Gulf Stream, and a spurious east-bound current near Azores heading toward the Gibraltar.

that the main influence on the PGF error is this feature, not the linearization of the compressibility terms in EOS. Despite the striking similarity of incompressible Cubic H errors (Fig. 15, lower left) and compressible, split-EOS (7.26), Cubic H errors (Fig. 16, lower left), these two methods actually produce quite different solutions under conditions of realistic temperature, salinity and forcing, where, in addition to small hydrostatic error, the scheme should be accurate in the dynamically relevant PGF. Moreover, we will see that neglecting compressibility results in a completely wrong dynamical response.

Fig. 17 shows six-month averaged, near-surface currents from two different solutions for the Atlantic Ocean under realistic wind stress, heat, and fresh-water flux forcing, starting from a Levitus (θ, S) climatology and running for a three-year spin-up period before the time-averaging begins. The averaging period corresponds to the spring-summer season. Unlike the flat-stratification test problem, where there is no mixing of temperature and salinity, the realistic simulation cannot be made without material diffusion due to both physical and numerical reasons. So in all the realistically forced simulations reported here, fourth-order centered advection is replaced with third-order, upstream-biased advection, but still with no explicit horizontal diffusion. The KPP scheme is used as the parameterization of the vertical mixing processes, Large *et al*, 1994. The first solution uses the modified Cubic H PGF algorithm with harmonic averaging of adiabatic differences (7.26) of ρ and split EOS (7.20) with $n_{\max} = 1$ (i.e., the same combination as for Fig. 16, lower left). This combination produces what we consider a physically plausible result in the sense that all primary features—such as correct Gulf Stream separation point—are present and broadly consistent with measurements. The second solution differs from the first one only by turning OFF compressibility terms (the same EOS and PGF combination as in Fig. 15, lower left). Although qualitatively similar in its main features to the first solution, the second solution is characterized by an approximately 40% weaker and prematurely separating Gulf Stream, as well as a spurious eastward current near the Azores heading towards Gibraltar. We do not show the near-surface velocities from two other solutions — $\gamma = 0$ and $\gamma = 0.5$ schemes with EOS (7.14), which retains nonlinear compressibility, but does not contain passive vertical ρ gradient — with the exception of minor differences in Gulf Stream separation site, these are rather similar to the first solution on Fig. 17 and interpreting their differences is not straightforward. On the other hand, comparing the mid-depth currents from all four solutions is more informative since there are larger differences (Fig. 18). Among these solutions the one on the lower-right panel, [Cubic H + incompressible EOS], is anomalous among the others: it has a narrower and more intense Deep Western Boundary Current (DWBC), especially in the Gulf Stream area; a spurious current system off coast of Portugal, which extents towards the northwest; and a northward current along the African coast, which is completely absent on the other three solutions. Examination of temperature and salinity fields (not shown here) reveals that the spurious current off coast of Portugal is due to the response to the Mediterranean outflow[14] combined with erroneous α and β because of neglect of the thermobaric effect. When these two coefficients are correct, the PGF contributions due to temperature and salinity gradients approximately cancel each other, resulting in a very small PGF gradient (as occurs in the other three solutions), hence weak geostrophically balanced currents. In fact, under these conditions (as seen in Appendix B), α may be off by as much as 50%, if its compressibility dependence is neglected. As the simulation continues, the temperature and salinity fields adjust toward a new state, resulting in a different circulation—the narrow jet along the coast of Portugal continuing northwestward. This current advects the Mediterranean water northward along the coast, ultimately maintaining a strong cross-shore gradient, which maintains the current itself in a "self-locking" mechanism. No such current occurs in the solution shown on the right. Instead there is much weaker current going northwestward from Gibraltar, separating from the coast at approximately 38^0N, and heading toward the west. This is the expected behavior from observations, Haidvogel *et al*, 2000. The three remaining solutions—top left, top right, and lower left—are qualitatively similar to each other. This indicates that they are predominantly controlled by the underlying physics, not by their numerical errors, but there are still differences worth pointing out. The most striking distinction is the intensity of DWBC off the Brazilian coast.

POM scheme ($\gamma = 0$) gives approximately twice the peak velocity there and a noticeable increase in the energy (indicated by the increase in rms velocity from approximately 2.3 cm/sec to 3.0 cm/sec). The other two schemes—[Cubic H + (7.26)] and $\gamma = 0.5$—are quite similar by these measures. Comparison of these results with the flat-stratification test (cf., Fig. 15) suggests that a plausible explanation of the difference between $\gamma = 0$ and $\gamma = 0.5$ results in Fig. 18 lies in the hydrostatic PGF error: $\gamma = 0$ produces southward flow near the Brazilian coast in the flat stratification test problem, which is in the same direction as the stronger DWBC on Fig. 15. On the other hand, the hydrostatic error of $\gamma = 0.5$ is opposite to DWBC, which is consistent with its smaller velocities in the realistic forcing experiment. The overall sensitivity of DWBC to the choice of weighting parameter γ is comparable to the differences among the three major classes of models, z-, sigma-, and isopycnic coordinate, Beckmann, 1998, and Willebrand, *et al*, 2001. The DWBC results with [Cubic H + (7.26)] are in between the other two, but closer to $\gamma = 0.5$. Besides the intensity of the DWBC, Fig. 18 shows other differences between $\gamma = 0$ and $\gamma = 0.5$: the appearance of possibly spurious vortex structures off the African coast in the Gulf of Guinea and Canary Islands, as well as the generation of Rossby waves near the Equator manifested by alternating east-west bands in the velocity field, which are tracks of stronger, westward-traveling vortex structures in the case of $\gamma = 0$.

Making a firm conclusion about which of the three solutions is physically the most accurate is beyond the scope of this paper, so we merely point out that the sensitivity of the answers to the choices among the POM Jacobian and $\gamma = 0, ..., 0.5$ in the Song, 1998, family of schemes and the non-robustness of the "optimal" choice of γ in different configurations all motivate the search for higher-order alternatives, such as Cubic H. We also notice that evaluating a PGF scheme solely by its hydrostatic error, (i.e., the flat-stratification test problem) does not necessarily guarantee an accurate simulation in realistic cases. For example, POM Jacobian performs better than $\gamma = 0.5$ in the flat-stratification test shown on Fig. 15; however, $\gamma = 0$ results in the realistic simulation (Fig. 18) has

[14] In this model configuration Mediterranean outflow is simulated by specifying point-sources in the vicinity of Gibraltar Strait, where θ, S are artificially maintained at their climatological values.

Appendix A: On Discrete Energetic Consistency of High-Order PGF Schemes

Song & Wright, 1998, (hereafter SW98), show that the second-order equal-weighted[15] density-Jacobian scheme in combination with second-order, centered advection for density guarantees exact conservation of total (kinetic + potential) energy of the discretized system. In this Appendix we show that their derivation can be extended to a more general case where two-point, linear interpolation of ρ in both PGF and advection schemes is replaced with a more general, potentially high-order accurate interpolation. For brevity we present here only discrete equations. Reader should be refered to SW98 for their continuous prototypes.

Since both the original second-order and our new scheme can be rewritten in pseudo-flux form, the x-component of the PGF with sign and scaling as it appears in the r.h.s. of the finite-volume momentum equation for $u_{i+\frac{1}{2},k}$ is

$$PX_{i+\frac{1}{2},k} \equiv -\widetilde{\Delta H}^{x}_{i+\frac{1}{2},k} \left.\frac{\partial p}{\partial x}\right|_z = \widetilde{\Delta H}^{x}_{i+\frac{1}{2},k} \sum_{k'=k}^{N} \left(FX_{i,k'+\frac{1}{2}} - FX_{i+1,k'+\frac{1}{2}} + FCX_{i+\frac{1}{2},k'+1} - FCX_{i+\frac{1}{2},k'} \right) \tag{A.1}$$

$$= -\widetilde{\Delta H}^{x}_{i+\frac{1}{2},k} \left\{ \delta_x \left. \sum_{k'=k}^{N} FX_{k'+\frac{1}{2}} \right|_{i+\frac{1}{2}} + FCX_{i+\frac{1}{2},k} \right\} ,$$

where δ_x denotes elementary 2-point differencing over one grid interval, $\delta_x q_{i+\frac{1}{2}} = q_{i+1} - q_i$ and $\delta_x q_i = q_{i+\frac{1}{2}} - q_{i-\frac{1}{2}}$, hence the result is always placed half-way between the points at which the original quantity is defined. For notational simplicity we also assume a Cartesian grid with $\Delta x = \Delta y = 1$, and we omit the factor g/ρ_0 from the definitions of PGF and potential energy below; $\widetilde{\Delta H}^{x}_{i+\frac{1}{2},k}$ denotes height of control volume element surrounding $u_{i+\frac{1}{2},k}$, which in the simplest case can be approximated by second-order mid-point averaging $\widetilde{\Delta H}^{x}_{i+\frac{1}{2},k} = (\Delta H_{i,k} + \Delta H_{i+1,k})/2$, but in general it may be done by an arbitrary interpolation scheme, e.g., a fourth-order scheme. In any case $\Delta H_{i,k} = z_{i,k+\frac{1}{2}} - z_{i,k-\frac{1}{2}}$ is vertical spacing of arbitrarily stretched vertical grid, so neither $z_{i,k+\frac{1}{2}} \neq (z_{i,k} + z_{i,k+1})/2$ nor $z_{i,k} \neq \left(z_{i,k-\frac{1}{2}} + z_{i,k+\frac{1}{2}} \right)/2$; Further in (A.1) FX and FCX are "pseudo-fluxes" which in the simplest case are computed as

$$FX_{i,k+\frac{1}{2}} = \left. (\overline{\rho}^{s} \delta_s z) \right|_{i,k+\frac{1}{2}} \qquad \text{and} \qquad FCX_{i+\frac{1}{2},k} = \left. (\overline{\rho}^{x} \delta_x z) \right|_{i+\frac{1}{2},k} , \tag{A.2}$$

where $\overline{\rho}^{s}$ and $\overline{\rho}^{x}$ are mid-point averaged values of density. It is implied that the surface value $FCX_{i+\frac{1}{2},N+1} \equiv 0$ in the first line of (A.1). Model variables are placed on a C-grid and their permissible index ranges and boundary conditions are given by

$$\begin{array}{lllll} z, \rho_{i,j,k} & i = 1, \ldots, L & j = 1, \ldots, M & k = 1, \ldots, N & \\ u_{i+\frac{1}{2},j,k} & i = 0, \ldots, L & & & u_{\frac{1}{2},j,k} = u_{L+\frac{1}{2},j,k} = 0 \\ v_{i,j+\frac{1}{2},k} & & j = 0, \ldots, M & & v_{i,\frac{1}{2},k} = u_{i,M+\frac{1}{2},k} = 0 \\ \omega_{i,j,k+\frac{1}{2}} & & & k = 0, \ldots, N & \omega_{i,j,\frac{1}{2}} = \omega_{i,j,N+\frac{1}{2}} = 0 \,. \end{array} \tag{A.3}$$

After substitution of (A.2) into (A.1), the later becomes equivalent to Eq. (2.6) and, ultimately, (2.22) from SW98, with the exception of the top-most grid interval: it should be noted that Eqs. (2.6), (2.7), (2.22), and (2.25) from SW98 overshoot vertical index inside the summation by requiring values of ρ (b in their notation) and z at vertical index $N+1$ (via $\overline{b}^{s}_{N+\frac{1}{2}}$ and $\delta_s z_{N+\frac{1}{2}}$), which are not available. This means that a special rule for the computation of $FX_{N+\frac{1}{2}}$ is required to fix this problem. We do not specify this rule at this moment, but assume that $PX_{i+\frac{1}{2},N}$ can be still cast in pseudo-flux form[16].

In the following analysis we assume that instead of using (A.2), $FX_{i,k+\frac{1}{2}}$ and $FCX_{i+\frac{1}{2},k}$ are computed by an arbitrary, potentially high-order accurate, interpolation method. Another distinction from SW98 is that we do not

[15] also called *Standard Jacobian* in SW98

[16] Strictly speaking this is not the case for the POM and SCRUM models. Although to our best knowledge, the algorithm for computation of $PX_{i+\frac{1}{2},N}$ has never been published in the literature, it can be easily recovered from the code itself: $PX_{i+\frac{1}{2},N} = -\frac{1}{2} g \widetilde{\Delta H}^{x}_{i+\frac{1}{2},N} \left(\zeta_i - z_{i,N} + \zeta_{i+1} - z_{i+1,N} \right) \left(\rho_{i+1,N} - \rho_{i,N} \right)$, which simply neglects the fact that $\rho_{i+1,N}$ and $\rho_{i,N}$ are placed at different geopotential surfaces. (The finite-difference version of SPEM (v. 5.1) and SCRUM have a similar treatment.) Besides the usual "leak" of vertical stratification into horizontal PGF, this formulation does not provide pseudo-flux continuity between the elements N and $N-1$ of the vertical grid. In the derivation presented here we assume that both these drawbacks are repaired.

where $\widehat{\rho}^x_{i+\frac{1}{2},j,k}$ the result of mid-point interpolation of ρ (to the location of $u_{i+\frac{1}{2},j,k}$) using an arbitrary interpolation method, which is not necessarily linear and not necessarily the same for all directions x, y, s. Multiplying (A.9) by $z_{i,j,k}$ and applying summation by parts, we derive

$$\sum_{i=1}^{L}\sum_{j=1}^{M}\sum_{k=1}^{N} z_{i,j,k}\frac{\partial}{\partial t}\left(\Delta H_{i,j,k}\rho_{i,j,k}\right) = -\sum_{i=1}^{L}\sum_{j=1}^{M}\sum_{k=1}^{N} z_{i,j,k}\left\{\delta_x\left(\widehat{\rho}^x\cdot\widetilde{\Delta H}^x_k u_k\right)+\delta_y\left(\widehat{\rho}^y\cdot\widetilde{\Delta H}^y_k v_k\right)+\delta_s\left(\widehat{\rho}^s\cdot\omega\right)\right\}$$
$$= \sum_{i=1}^{L-1}\sum_{j=1}^{M}\sum_{k=1}^{N}\widehat{\rho}^x_{i+\frac{1}{2},j,k}\cdot\widetilde{\Delta H}^x_{i+\frac{1}{2},j,k}u_{i+\frac{1}{2},j,k}\delta_x z_{i+\frac{1}{2},j,k} \tag{A.10}$$
$$+\sum_{i=1}^{L}\sum_{j=1}^{M-1}\sum_{k=1}^{N}\widehat{\rho}^y_{i,j+\frac{1}{2},k}\cdot\widetilde{\Delta H}^y_{i,j+\frac{1}{2},k}v_{i,j+\frac{1}{2},k}\delta_y z_{i,j+\frac{1}{2},k}+\sum_{i=1}^{L}\sum_{j=1}^{M}\sum_{k=1}^{N-1}\widehat{\rho}^s_{i,j,k+\frac{1}{2}}\cdot\omega_{i,j,k+\frac{1}{2}}\delta_s z_{i,j,k+\frac{1}{2}}\,.$$

Also note that

$$\sum_{i=1}^{L}\sum_{j=1}^{M}\sum_{k=1}^{N} z_{i,j,k}\frac{\partial}{\partial t}\left(\Delta H_{i,j,k}\rho_{i,j,k}\right) = \underbrace{\frac{\partial}{\partial t}\sum_{i=1}^{L}\sum_{j=1}^{M}\sum_{k=1}^{N} z_{i,j,k}\Delta H_{i,j,k}\rho_{i,j,k}}_{\frac{dPE}{dt}} - \sum_{i=1}^{L}\sum_{j=1}^{M}\sum_{k=1}^{N}\Delta H_{i,j,k}\rho_{i,j,k}\frac{\partial z_{i,j,k}}{\partial t} \tag{A.11}$$

Comparison of (A.10) with (A.5), along with (A.8) and (A.11), indicates that in order to guarantee energetic consistency,

$$\left.\frac{dKE}{dt}\right|_{PGF}+\frac{dPE}{dt}=0\,, \tag{A.12}$$

it is sufficient to ensure that

$$\begin{array}{llll} FX_{i,j,k+\frac{1}{2}} = \widehat{\rho}^s_{i,j,k+\frac{1}{2}}\delta_s z_{i,j,k+\frac{1}{2}} & \text{for all} & & k=1,\dots,N-1 \\ FCX_{i+\frac{1}{2},j,k} = \widehat{\rho}^x_{i+\frac{1}{2},j,k}\delta_x z_{i+\frac{1}{2},j,k} & \text{everywhere,} & \text{where} & u_{i+\frac{1}{2},j,k}\neq 0 \\ FCY_{i,j+\frac{1}{2},k} = \widehat{\rho}^y_{i,j+\frac{1}{2},k}\delta_y z_{i,j+\frac{1}{2},k} & \text{everywhere,} & \text{where} & v_{i,j+\frac{1}{2},k}\neq 0\,, \end{array} \tag{A.13}$$

and

$$-\sum_{k=1}^{N} FX_{i,j,k+\frac{1}{2}}\frac{\partial z_{i,j,k+\frac{1}{2}}}{\partial t}+\sum_{k=1}^{N}\Delta H_{i,j,k}\rho_{i,j,k}\frac{\partial z_{i,j,k}}{\partial t}=0\,, \tag{A.14}$$

which leads to the following set of conclusions:

- Discrete energetic consistency can be shown if: (*i*) discrete PGF scheme can be written in pseudo-flux form; and (*ii*) ρ used in PGF is the same, or linearly related to that in the advection equation; and (*iii*) interpolation algorithms used in computation of pseudo-fluxes FX, FCX, and FCY are the same as corresponding interpolations in discrete advection for density. Details of the vertical coordinate (such as vertical stretching or order of interpolation) to compute $\widetilde{\Delta H}^x_{i+\frac{1}{2},j,k}$ from $\Delta H_{i,j,k}$ do not destroy the consistency, as long as the same method is used in continuity, density, and momentum equations.
- The second-order scheme corresponds to the setting of $\widehat{\rho}^x_{i+\frac{1}{2},j,k}=\overline{\rho}^x_{i+\frac{1}{2},j,k}$ in (A.13) (similarly in other two directions), which is energetically consistent. Alternatively one can chose

$$\widehat{\rho}_{i+\frac{1}{2},j,k}=-\frac{1}{16}\rho_{i-1,j,k}+\frac{9}{16}\rho_{i,j,k}+\frac{9}{16}\rho_{i+1,j,k}-\frac{1}{16}\rho_{i+2,j,k} \tag{A.15}$$

  or even a more sophisticated method (e.g., using harmonic averaging of elementary slopes to prevent spurious oscillations) and still retain energetic consistency. However, no choice results in fourth-order accuracy for both

The usual argument in favor of using an energetically consistent pair of PGF and advection schemes is based on oceanic simulations being typically long-term integrations, so that one can be fearful of accumulation of erroneous energy conversion even when it is within the numerical order of accuracy at each time step. However, the potential energy defined above is computed with respect to a state where all mass is concentrated at $z = 0$, i.e., the unperturbed free surface. This state is not achievable, because PE is defined without taking into account constraints of incompressibility and Lagrangian conservation of density. A more physically meaningful definition of potential energy is *available potential energy* (APE), which respects both these constraints. The main argument behind this concept lies in the fact that as long as fluid parcels are move up and down while maintaining their density, potential energy released in such rearrangement is converted into kinetic energy, and once a state in which each fluid parcel is in hydrostatic equilibrium with its surrounding is achieved, no more potential energy can be released. Although exact Eulerian mass conservation is often imposed in oceanic models, maintaining ρ for each Lagrangian parcel is usually possible only within the numerical accuracy of the advection scheme[18]. This leads to a situation in which an energetically consistent pair does not guarantee the absence of spurious generation of kinetic energy, because numerical advection can alter PE and APE in a nonphysical way (via advective errors), making it available for KE production while maintaining $KE+PE$. This agrees with practical experience to date, where one can modify either PGF or advection independently (thus abandoning exact $KE + PE$ conservation) and observe an overall beneficial outcome for the accuracy of model solution.

Appendix B: Assessment of Taylor Expansion for Seawater Compressibility

To facilitate our analysis we rewrite seawater EOS from Jackett & McDougall, 1995 (hereafter JM95) as

$$\rho_{\text{in situ}}\left(\theta,S,z\right) = \frac{\rho_0+\rho_1'\left(\theta,S\right)}{1-0.1z/\left[K_{00}+K'\left(\theta,S,z\right)\right]} = \frac{\rho_0}{1-0.1z/K_{00}}+\rho_1'+\frac{0.1z}{K_{00}+K'-0.1z}\left[\rho_1'-\frac{\rho_0 K'}{K_{00}-0.1z}\right], \quad \text{(B.1)}$$

so far without any approximation. Here $\rho_0 = const$, $K_{00} = const$, $K' = K_0' + K_1 z + K_2 z^2$, where $K_0 = K_0\left(\theta,S\right)$, $K_1 = K_1\left(\theta,S\right)$, $K_2 = K_2\left(\theta,S\right)$, as well as $\rho_1' = \rho_1'\left(\theta,S\right)$ are expressed in as polynomials of powers of θ, S and $S^{1/2}$; $z > 0$ is depth, which in the context of EOS substitutes for *in situ* pressure $P = \rho_0 g z$ (thus neglecting nonuniformity of ρ field when computing compressibility effects); $\rho_0 = 1000\,\text{kg/m}^3$ is reference density; and $g = 9.81\text{m/s}^2$ is acceleration of gravity. Since $\rho_1' \ll \rho_0 = const$ with an associated small parameter $\rho_1'/\rho_0 \le 3\times10^{-3}$, and since

$$0.1z\,,\ K_1 z \ll K_0 \equiv K_{00}+K_0'\,, \qquad K_0' \le K_{00}\,, \quad \text{and} \quad K_2 z^2 \le K_1 z\,, \quad \text{(B.2)}$$

the r.h.s of (B.1) is dominated by its first term, $\rho_0/(1-0.1z/K_{00})$, which does not contribute to the horizontal PGF, because it is a function of z only. The smallness of the leftmost inequality in (B.2) can be estimated from a typical value speed of sound c of seawater,

$$\frac{1}{c^2} = \left.\frac{\partial\rho}{\partial p}\right|_{\theta,S} = \frac{1}{\rho_0 g}\left.\frac{\partial\rho}{\partial p}\right|_{\theta,S} \approx \frac{1}{\rho_0 g}\cdot\frac{0.1\rho_0}{K_0}\,, \quad \text{hence} \quad \frac{0.1z}{K_0} = \frac{gz}{c^2} = \frac{9.81\cdot 6\times10^3}{1500^2} = 2.5\times10^{-2}\,, \quad \text{(B.3)}$$

where we use $z = 6000$m, and $c = 1500\text{m/s}^2$ for this estimate. The terms $0.1z$ and $K_1 z$ are assumed to be of the same order. The other two inequalities in (B.2) mean that terms proportional to z and z^2 never dominate K_0. Furthermore, $K_0\left(\theta,S\right) = K_{00} + K_0'\left(\theta,S\right) \approx 19092.6 + 209.8\theta + 104.4S + ...$, hence $K_0' \le K_{00} = const$ in the sense that terms dependent on θ and S never dominate the preceding K_{00}; however, they are not sufficiently small to be used in a Taylor expansion accurate enough for practical purposes. This estimate also explains why removing a background $\rho(z)$ profile, essentially $\rho_0/(1-0.1z/K_{00})$, has only limited success in reducing PGF errors.

Retaining only terms which contribute to horizontal PGF and using the two small parameters identified above, the Taylor series expansion of (B.1) results in

$$\rho\left(\theta,S,z\right) = \rho_1' + 0.1\frac{\rho_1'-\rho_0 K_0'/K_{00}}{K_{00}+K_0'}z - 0.1\left(\rho_0+\rho_1'\right)\frac{K_1-0.1}{\left(K_{00}+K_0'\right)^2}z^2 + \mathcal{O}\left(\left(\frac{z}{K_0}\right)^3\right) = \rho_1' + q_1 z + q_2 z^2\,, \quad \text{(B.4)}$$

[18] With the exception of isopycnic-coordinate models, where it can be done exactly by conserving the volume of each isopycnal layer.

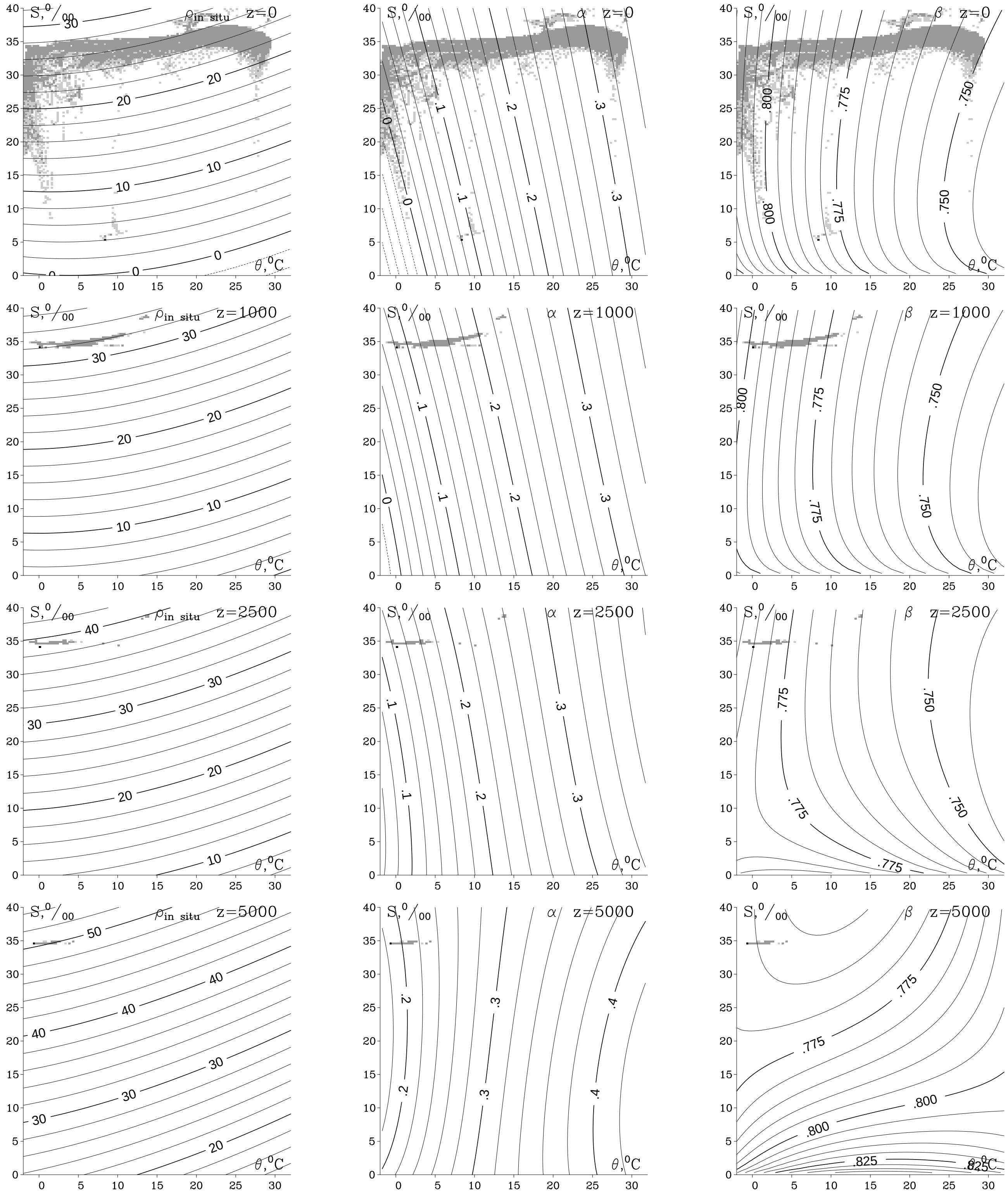

Figure 19. Density *in situ* ρ **(left)**, thermal expansion α **(middle)** and saline contraction coefficient β **(right)** as functions of potential temperature θ and salinity S at four different depths $z = 0$, 1000, 3000 and 6000 m. Light shading indicates availability (at least one record) of water with given temperature and salinity at each specified depth from annual database for World Ocean, Levitus 1994, while dark shading correspongs to the area containing at least 90% of all data at specified depth. Thermobaric effect is manifested by the change of angle of isopycnals with depth on $\rho\,(\theta, S)$ plot, left column.

References

Arakawa, A., and M. J. Suarez, 1983, Vertical differencing of the primitive equations in sigma coordinates. *Monthly Weather Review*, **111**, 34-45.

Beckmann, A., and D. B. Haidvogel, 1993: Numerical simulation of flow around a tall isolated seamount. Part. 1: Problem formulation and model accuracy. *Journ. Phys. Ocean.*, **23**, 1736-1753.

Beckmann, A., and D. B. Haidvogel, 1997: A numerical simulation of flow at Fieberling Guyot. *Journ. Geophys. Res.*, **102**, 5595-5613.

Beckmann, A., 1998: The representation of bottom boundary layer processes in numerical ocean circulation models. in *Ocean modeling and Parametrization*, E. P. Chassignet & J. Verron, editors. *Kluwer Acad. Pub.*, pp. 135-154.

Blumberg, A. F. and G. L. Mellor, 1987: A description of a three-dimensional coastal ocean circulation model. In *Three-dimensional Coastal Ocean Models*, ed. N. Heaps (Pub. AGU), pp. 1-16.

Chu, P. C. and C. Fan, 1997: Sixth-order difference scheme for sigma coordinate ocean models. *Journ. Phys. Ocean.*, **27**, 2064-2071.

Chu, P. C. and C. Fan, 1998: A three-point combined compact difference scheme. *Journ. Comp. Phys.*, **140**, 370-399.

Dukowicz, J. K., 2001: Reduction of density and pressure gradient errors in ocean simulations. *Journ. Phys. Ocean.*, **31**, 1915-1921.

Gary, J. M., 1973: Estimate of truncation error in transformed coordinate primitive equation atmospheric models. *Journ. Atmosph. Sci.*, **30**, 223-233.

Gerdes, R., 1993: A primitive equation ocean circulation model using a general vertical coordinate transfornmation. 1. Description

Haidvogel, D. B., H. Arango, K. Hedstrom, A. Beckmann, P. Rizzoli and A. F. Shchepetkin, 2000: Model evaluation experiments in the North Atlantic Basin: Simulations in non-linear terrain-following coordinates. *Dyn. Atmos. Oceans*, **32**, 239-281.

Haidvogel, D. B., A. Beckmann, D. C. Chapman, and R.-Q. Lin, 1993: Numerical simulation of flow around a tall isolated seamount: Part II: Resonant generation of trapped waves. *Journ. Phys. Ocean.*, **23**, 2373-3291.

Haidvogel, D. B., and A. Beckmann, 1999: Numerical Ocean Modeling. *Imperical College Press.*, London, 330 pages.

Haney, R. L., 1991: On the pressure gradient force over steep topography in sigma coordinate ocean models. *Journ. Phys. Ocean.*, **21**, 610-618.

Jackett, D. R. and T. J. McDougall, 1995: Minimal Adjustment of Hydrostatic Profiles to Achieve Static Stability. *Journ. Atmos. Oceanic Technology*, **12**, 381-389.

Janjic, Z. I., 1977: Pressure gradient force and advection scheme used for forecasting with steep and small scale topography. *Contrib. Atmos. Phys.*, **50**, 186–199.

Janjic, T., 1998: Comments on "A finite volume integration method for computing pressure gradient force in general vertical coordinates", *Q. J. R. Meteorol. Soc.,*, **124**, 2527–2529.

Kliem, N., and J. D. Pietrzak, 1999: On the pressure gradient errors in sigma coordinate ocean models: A comparison with laboratory experiments. *Journ. Geophys. Res.*, **104**, 29,781-29,799.

Large, W. G., J. C. McWilliams, and S. C. Doney, 1994: Oceanic vertical mixing: A review and a model with a nonlocal boundary layer parametrization. *Reviews Geophys.*, **32,4**, 363-403.

Leer, van B., 1977: Towards the Ultimate Conservative Difference Scheme III. Upstream-centered Finite-Difference Schemes for Ideal Compressible Flow. *Journ. Comp. Phys.*, **23**, 263-275.

Lin, Shian-Jiann, 1997: A finite volume integration method for computing pressure gradient force in general vertical coordinates. *Q. J. R. Meteorol. Soc.,*, **123**, 1749-1762.

Lin, Shian-Jiann, 1998: Reply to comments by T. Janjic on "A finite volume integration method for computing pressure gradient force in general vertical coordinates", *Q. J. R. Meteorol. Soc.,*, **124**, 2531–2533.

Mahrer, Y., 1984: An improved numerical approximation of the horizontal pressure gradients in a terrain-following coordinate system. *Monthly Weather Review*, **112**, 918-922

McCalpin, J. D., 1994: A comparison of second-order and fourth-order pressure gradient algorithms in a σ-coordinate ocean model. *Int. J. of Num. Meth. in Fluids*, **18** , 361-383.